TKK Dissertations 174
Espoo 2009

MINIATURE PASSIVELY Q-SWITCHED LASERS AND THEIR APPLICATION TO NONLINEAR FREQUENCY CONVERSION IN MICROSTRUCTURED OPTICAL FIBER

Doctoral Dissertation

Esa Tapani Räikkönen

Helsinki University of Technology
Faculty of Information and Natural Sciences
Department of Applied Physics

TKK Dissertations 174
Espoo 2009

MINIATURE PASSIVELY Q-SWITCHED LASERS AND THEIR APPLICATION TO NONLINEAR FREQUENCY CONVERSION IN MICROSTRUCTURED OPTICAL FIBER

Doctoral Dissertation

Esa Tapani Räikkönen

Dissertation for the degree of Doctor of Science in Technology to be presented with due permission of the Faculty of Information and Natural Sciences for public examination and debate in Large Seminar Hall of Micronova at Helsinki University of Technology (Espoo, Finland) on the 7th of August, 2009, at 12 noon.

Helsinki University of Technology
Faculty of Information and Natural Sciences
Department of Applied Physics

Teknillinen korkeakoulu
Informaatio- ja luonnontieteiden tiedekunta
Teknillisen fysiikan laitos

Distribution:
Helsinki University of Technology
Faculty of Information and Natural Sciences
Department of Applied Physics
P.O. Box 3500
FI - 02015 TKK
FINLAND
URL: http://tfy.tkk.fi/
Tel. +358-9-451 3153
Fax +358-9-451 3155
E-mail: esa.raikkonen@tkk.fi

ISBN 978-951-22-9982-9
ISBN 978-951-22-9983-6 (PDF)
ISSN 1795-2239
ISSN 1795-4584 (PDF)
URL: http://lib.tkk.fi/Diss/2009/isbn9789512299836/

TKK-DISS-2624

Multiprint Oy
Espoo 2009

ABSTRACT OF DOCTORAL DISSERTATION

HELSINKI UNIVERSITY OF TECHNOLOGY
P. O. BOX 1000, FI-02015 TKK
http://www.tkk.fi

Author Esa Tapani Räikkönen

Name of the dissertation

Miniature passively Q-switched lasers and their application to nonlinear frequency conversion in microstructured optical fiber

Manuscript submitted 10.3.2009	Manuscript revised
Date of the defence 7.8.2009	
☐ Monograph	☒ Article dissertation (summary + original articles)

Faculty	Faculty of Information and Natural Sciences
Department	Department of Applied Physics
Field of research	Optics
Opponent(s)	Professor Valdas Pasiskevicius
Supervisor	Professor Matti Kaivola
Instructor	Ph.D. Scott C. Buchter

Abstract

Laser devices are an integral part of the technological background of our modern society. Laser light transmits data over the fiber-optical cabling of internet, reads DVD disks and bar codes, cuts metals and plastics, etc. Many applications, such as refractive eye surgery, breakdown spectroscopy, and various time-resolved methods, rely on optical power that is delivered in short pulses. The bite of laser light on matter is also greatly enhanced by pulsing.

Q-switching is a method of producing pulsed laser light by periodically suppressing the optical feedback of a laser resonator. In passive Q-switching the cycle is run without any external control by the process of saturable absorption. Miniature passively Q-switched lasers are small solid-state devices that produce nanosecond long, kilowatt peak power pulses of coherent light at near-infrared wavelengths. They are simple to fabricate and have found applications, e.g., in range finding, micro machining and spectroscopy.

In this thesis the operation of miniature passively Q-switched lasers is studied both theoretically and experimentally. Also, nonlinear frequency conversion of the laser output is applied in microstructured optical fiber. The conversion allows for the laser output to be extended into wavelengths at which no laser sources exist. In miniature lasers the cavity decay time and the thermalization time of the laser multiplets are at close to equal. In order to take this into account, the normalized geometric rate-equation model of passively Q-switched lasers is refined to include the thermalization process. As an experimental case, a high peak power 1123 nm Nd:YAG laser is demonstrated, and the nonsaturable loss level of the Cr:YAG saturable absorber crystal is measured at the laser's wavelength.

The output spectrum of a passively Q-switched and frequency-doubled Nd:YAG laser is converted to narrowband visible light ranging from blue to red wavelengths by means of nondegenerate four-wave mixing, and to a broad spectrum of blue light by means of cascaded cross-phase modulation. The output spectra are adjusted by the group-delay profile of the microstructured optical fiber. A broadband source continuously covering the wavelength range of 420–1300 nm is realized by pumping a microstructured optical fiber with a miniature gain-switched Ti:Sapphire laser.

Keywords solid-state lasers, Q-switching, nonlinear fiber optics

ISBN (printed) 978-951-22-9982-9	ISSN (printed) 1795-2239
ISBN (pdf) 978-951-22-9983-6	ISSN (pdf) 1795-4584
Language English	Number of pages 76 p. + app. 32 p.

Publisher Helsinki University of Technology, Department of Applied Physics

Print distribution Helsinki University of Technology, Department of Applied Physics

☒ The dissertation can be read at http://lib.tkk.fi/Diss/2009/isbn/9789512299836

VÄITÖSKIRJAN TIIVISTELMÄ	TEKNILLINEN KORKEAKOULU PL 1000, 02015 TKK http://www.tkk.fi

Tekijä Esa Tapani Räikkönen

Väitöskirjan nimi

Pienikokoiset passiivisesti Q-kytketyt laserit ja epälineaarinen optinen taajuusmuunnos mikrorakenteisessa optisessa kuidussa

Käsikirjoituksen päivämäärä 10.3.2009	Korjatun käsikirjoituksen päivämäärä
Väitöstilaisuuden ajankohta 7.8.2009	
☐ Monografia	☒ Yhdistelmäväitöskirja (yhteenveto + erillisartikkelit)

Tiedekunta	Informaatio- ja luonnontieteiden tiedekunta
Laitos	Teknillisen fysiikan laitos
Tutkimusala	Optiikka
Vastaväittäjä(t)	Professor Valdas Pasiskevicius
Työn valvoja	Professori Matti Kaivola
Työn ohjaaja	Ph.D. Scott C. Buchter

Tiivistelmä

Laserlaitteet ovat oleellinen osa modernin yhteiskuntamme taustalla vaikuttavaa tekniikkaa. Laservalon avulla voidaan välittää tietoa kuituoptisissa verkoissa, lukea DVD-levyjä ja viivakoodeja, työstää metalleja ja muoveja, jne. Useat sovelluskohteet, kuten silmäkirurgia, laser-indusoitu plasmaspektroskopia ja monet aikatason menetelmät perustuvat pulssitettuun laservaloon. Pulssitus lisää myös huomattavasti laservalon kykyä työstää materiaaleja.

Q-kytkennäksi kutsutaan menetelmää, jolla tuotetaan laservalon pulsseja vaimentamalla jaksollisesti laserresonaattorin optista takaisinkytkentää. Passiivisessa Q-kytkennässä jaksotus syntyy ilman ulkoista ohjausta perustuen optisen absorption kyllästymisilmiöön. Pienikokoiset passiivisesti Q-kytketyt laserit tuottavat noin nanosekunnin pituisia, kilowattiluokan valopulsseja infrapuna-aallonpituuksilla. Niitä on yksinkertaista valmistaa, ja ne ovat löytäneet monia sovelluskohteita etäisyyden mittaamisessa, mikrotyöstössä ja spektroskopiassa.

Väitöstyössä on tutkittu pienikokoisia passiivisesti Q-kytkettyjä lasereita, niiden numeerista mallintamista, sekä epälineaarisia menetelmiä pulssien taajuuden muokkaamiseksi mikrorakenteisessa optisessa kuidussa. Resonaattorin lyhyen pituuden seurauksena valon poistuma-aika kaviteetista on näillä lasereilla samaa luokkaa kuin vahvistavan aineen termalisaatioaika. Tämä on otettu huomioon lisäämällä normitettuun geometriseen taseyhtälömalliin vahvistavan aineen termalisaatioprosessi. Työssä on myös kehitetty suuren huipputehon 1123 nm Nd:YAG-laser, ja määritetty käytetyn Cr:YAG-Q-kytkimen kyllästymättömät häviöt kyseisellä aallonpituudella.

Työssä esitetään, kuinka epädegeneroidulla neliaaltosekoituksella voidaan muuntaa osa taajuuskahdennetun ja passiivisesti Q-kytketyn Nd:YAG-laserin pulssista kapeakaistaiseksi näkyväksi valoksi, joka ulottuu sinisestä punaiseen, sekä kuinka ristikkäisvaihemodulaatiolla voidaan vastaavasti tuottaa laajakaistaista sinistä valoa. Synnytetyt aallonpituudet määräytyvät käytetyn mikrorakenteisen optisen kuidun ryhmänopeuskäyrän perusteella. Lisäksi esitetään, kuinka voidaan tuottaa erittäin laajakaistaista valoa aallonpituuksilla 420–1300 nm muuntamalla pienikokoisen pulssipumpatun titaanisafiirilaserin pulssin valon taajuus mikrorakenteisessa optisessa kuidussa.

Asiasanat kiinteän olomuodon laserit, Q-kytkentä, epälineaarinen kuituoptiikka

ISBN (painettu) 978-951-22-9982-9	ISSN (painettu) 1795-2239
ISBN (pdf) 978-951-22-9983-6	ISSN (pdf) 1795-4584
Kieli Englanti	Sivumäärä 76 s. + liit. 32 s.

Julkaisija Teknillinen korkeakoulu, Teknillisen fysiikan laitos

Painetun väitöskirjan jakelu Teknillinen korkeakoulu, Teknillisen fysiikan laitos

☒ Luettavissa verkossa osoitteessa http://lib.tkk.fi/Diss/2009/isbn/9789512299836

Preface

The research presented in this dissertation has been performed in the laboratory of Optics and Molecular Materials at Helsinki University of Technology, in close collaboration with the Arctic Photonics Ltd. The financial support from the Graduate School of Modern Optics and Photonics, the Finnish Foundation for Technology Promotion, and Emil Aaltonen Foundation is kindly acknowledged.

I would like to thank the supervisor of my work, Professor Matti Kaivola, for offering the place of a graduate student in his laboratory and the necessary hardware for carrying out the research. Professor Kaivola had always time for discussing the matter at hand. For all time I'll be grateful to my instructor Scott C. Buchter, who taught me the art of laser building. My work would not have been possible without his guidance at the beginning and the fruitfull discussions later on.

Great many people have contributed to the process leading to this thesis. I would like to acknowledge Markus Hautakorpi for discussions with respect to fiber optics, Goëry Genty for performing the numerical simulations of supercontinuum generation and excellent advise on cross-phase modulation, Ossi Kimmelma and Miika Heiliö for collaboration with the laser sources, and Outi Reentilä for her samples of semiconductor-saturable absorber mirrors. I would especially like to thank Kim P. Hansen and his employer, Crystal Fibre Ltd., for providing the microstructured optical fiber.

Last, but not least, I would like to thank my wife Eiri for her support on my graduate studies and our newborn daughter Elsi for kicking me forward at the final stages of the thesis work.

Otaniemi, March 2009

Esa Räikkönen

List of publications

This thesis consists of an overview and the following publications in peer-reviewed journals:

I E. Räikkönen, S. C. Buchter, and M. Kaivola, ”Modeling the time dynamics of miniature passively Q-switched lasers,” Accepted for publication in IEEE Journal of Quantum Electronics, 2009.

II E. Räikkönen, O. Kimmelma, M. Kaivola, and S. C. Buchter, ”Passively Q-switched Nd:YAG/KTA laser at 561 nm,” Optics Communications **281**, 4088–4091, 2008.

III E. Räikkönen, S. C. Buchter, and M. Kaivola, ”Generation of monochromatic visible light in microstructured optical fiber by nondegenerate four-wave mixing,” Applied Physics B - Laser and Optics **91**, 461–465, 2008.

IV E. Räikkönen, M. Kaivola, and S. C. Buchter, ”Compact supercontinuum source for the visible using gain-switched Ti:Sapphire laser as pump,” Journal of the European Optical Society: Rapid Publications **1**, 06012, 2006.

V E. Räikkönen, G. Genty, O. Kimmelma, M. Kaivola, K. P. Hansen, and S. C. Buchter, ”Supercontinuum generation by nanosecond dual-wavelength pumping in microstructured optical fibers,” Optics Express **14**, 7914–7923, 2006.

These papers are referred to by their Roman numerals throughout the overview.

Author's contribution

The work summarized in this dissertation falls in the fields of solid-state laser physics and nonlinear fiber optics. It has been carried out in the laboratory of Optics and Molecular Materials at Helsinki University of Technology during the years 2004–2009, in collaboration with Arctic Photonics Ltd.

The authors contribution to the publications included in this thesis is:

I The author has constructed the model, performed the numerical calculations and analysis, conducted the experimental measurements, and written the paper.

II The author has composed the work, constructed the experimental setup and performed the measurements together with O. Kimmelma, and written the paper.

III The author has composed the work, constructed the experimental setup, performed the measurements, and written the paper.

IV The author has constructed the experimental setup, performed the measurements, and written the paper.

V The author has constructed the experimental setup together with S. C. Buchter, performed the measurements, and written the paper together with G. Genty.

Abbreviations

AR	Anti reflection
CW	Continuous wave
ESA	Excited state absorption
GSA	Ground state absortion
FWHM	Full width at half maximum
FWM	Four-wave mixing
HR	High reflection
HT	High transmission
IR	Infrared
MOF	Microstructured optical fiber
MPQ	Miniature passively Q-switched
NA	Numerical aperture
SC	Supercontinuum
SHG	Second harmonic generation
SESAM	Semiconductor saturable absorber mirror
UV	Ultraviolet
YAG	Yttrium aluminium garnet
XPM	Cross-phase modulation
ZDW	Zero dispersion wavelength

Symbols

α	σ_{gsa}/σ
α_p	Absorption coefficient of pump light
f_x	Fractional Boltzmann occupation factor of a laser level
c	Speed of light
h	Planck contant
k	Boltzmann constant
λ_l	Laser wavelength
λ_p	Pump wavelength
l	Length of gain medium
l_s	Length of saturable absorber
L_{cav}	Length of laser cavity
L	Round-trip dissipative loss of laser cavity
ω	Angular frequency
ϕ	Photon density
ϕ_N	Photon number
Φ	Normalized photon density
R	Reflectivity of output coupling mirror
R_c	Radius of curvature of output coupling mirror
r	Radial coordinate
σ	Spectroscopic laser emission cross-section
σ_e	Effective laser emission cross-section
σ_{gsa}	Ground state absorption cross-section of saturable absorber
σ_{esa}	Excited state absorption cross-section of saturable absorber
T_0	Unsaturated transmission of saturable absorber
τ_f	Fluorescence lifetime
t_r	Cavity round-trip time
Δt	Full-width-at-half-maximum (FWHM) pulse width
w_x	$1/e^2$-radius of a laser beam
z	Longitudinal coordinate
z_R	Rayleigh range of laser beam
ξ_a	Absorption efficiency of pump light
ξ_g	Conversion efficiency of gain-switched laser

Contents

1 Introduction

Miniature passively Q-switched (MPQ) lasers are small and robust sources of pulsed laser light [1, 2]. They consist of a solid-state gain medium and an optical switch which are placed in a couple of millimeters long optical resonator composed of two mirror surfaces. An external laser diode is used for exciting the active ions of the gain medium. At the opening of the switch the stored energy is released in a light pulse of typically nanosecond in length and kilowatts in peak power. MPQ lasers have found use in diverse applications such as range finding, micro machining, spectroscopy, and in seeding nonlinear fiber-optical devices [1–5].

In this thesis, understanding of the pulsing dynamics of miniature passively Q-switched lasers is improved by both experimental and theoretical work, and novel nonlinear techniques for extending the emission wavelength range of these lasers are demonstrated. Although passively Q-switched lasers are conceptually simple, their dynamical behavior is complicated and potentially chaotic [6]. In miniature lasers the pulse buildup occurs in a similar timescale as the thermalization of the laser transition's energy levels in the gain medium [7]. In this work a normalized radially-dependent rate-equation model that takes into accout the thermalization process is proposed and analyzed [7–9]. Improving the numerical model of the laser operation allows for a more accurate and faster design process. As an example, a MPQ laser making use of the low-gain 1123 nm transition of the Nd^{3+}:YAG laser crystal is demonstrated.

The output wavelength of a laser is defined by the energy of the laser transition in the gain medium and the optical feedback of the resonator. In MPQ lasers the gain is provided by a piece of crystal or glass that is doped with a small fraction of rare-earth ions such as Neodymium, Ytterbium, or Erbium. Optical transitions in rare-earth ions are characterized by long lifetimes of the excited state, allowing for efficient storage of the pulse energy in Q-switched operation, and implying a narrow line width. Their wavelengths lie mainly in the invisible infrared part of the spectrum [10].

Applications often call for a certain wavelength that is not among the existing laser wavelengths, and a need for frequency conversion of the laser output arises. Optical frequency conversion is based on nonlinear interaction between light and matter. It can be performed in bulk medium or in a waveguide such as the optical fiber. MPQ lasers produce high enough peak power for efficient single-pass harmonic generation in nonlinear

crystals [11], offering a simple way for increasing the number of available wavelengths. Waveguides however have the benefit of longer interaction length, so that nonlinear optical processes that would be too weak to be observed in bulk medium can be exploited.

In this thesis methods of nonlinear frequency conversion of MPQ laser output are studied in a novel type of an optical waveguide called the microstructured optical fiber (MOF). A MOF can feature both high effective nonlinearity and large tunable dispersion, making it a versatile medium that allows for both high conversion efficiency in a short length and control over which new wavelengths are created. Special emphasis is put on the generation of visible wavelengths ($\lambda = 0.4 - 0.7$ μm) due to the lack of compact pulsed laser sources in this wavelength range. Both narrowband frequency conversion and methods of generating extremely broadband spatially coherent light are demonstrated. Coupling high peak power pulses into a microstructured optical fiber can produce so-called "supercontinuum" (SC) light which has very broad spectrum and is directional and bright as laser light [12–14]. Applications of SC light are found in multispectral imaging, spectroscopic gas sensing, confocal microscopy, and optical coherence tomography, to name a few [15–18]. The well defined laser-like beam of white light is also visually very aesthetic, and it disperses into uniquely saturated colours in a prism.

The structure of the thesis is as follows: Chapter 2 discusses the various design aspects of miniature passively Q-switched lasers, and Chapter 3 is devoted to their numerical modeling. Chapter 4 reviews the structure and properties of microstructured optical fibers. In Chapter 5, the nonlinear frequency conversion in optical fiber with nanosecond long pump pulses is covered. Conclusions and future prospects are found in Chapter 6. This overview and the research articles [I–V] are complementary to each other, and emphasis is put on collecting together a broader background of the research than is possible in the individual papers.

2 Miniature passively Q-switched lasers

Lasers have made a breakthrough into our every-day life. They are found in video disc players, printers, pointers, bar-code readers, and they transmit the data on the physical layer of the Internet. All these applications rely on semiconductor lasers that are very cheap to mass produce. Semiconductor lasers have however not totally replaced other laser types due to the limitations in beam quality at high power operation and their inability to produce pulses of large energy. These are the operation conditions at which solid-state lasers shine. Still, the energy into a modern solid-state laser is provided by a semiconductor laser, because it can produce narrow-bandwidth, high brightness light that is efficiently absorbed by the solid-state laser material.

The availability of high brightness laser diodes has made possible the development of miniature solid-state lasers [19, 20]. A typical high-brightness laser diode with an emitter size of 1×100 μm can produce 3 watts of light at a wavelength of $\lambda \sim 0.8$ μm in the infrared. About half of this power can be converted into a good quality laser beam in a laser cavity which is only a few millimeters in length and houses a laser mode of the approximate diameter of that of the human hair, 100 μm.

Many solid-state laser materials can store the absorbed pump energy for a time of some hundreds of microseconds [10]. Thus, a decent amount of energy can be accumulated into the solid-state gain medium from the laser diode. A 3 W laser diode puts out 300 μJ of energy in a time of 100 μs. If only 10% of this energy could be released in a pulse of 10 ns in length, a pulse with a peak power of 3 kW would be obtained. With a beam diameter of 100 μm, this corresponds to an intensity of 40 megawatts per square centimeter. Inside the laser resonator the intensity is even an order of magnitude larger, and the damage threshold of the cavity components often becomes the limiting factor of the laser design.

Q-switching is a method of pulsing the laser output by placing a time variable loss inside the laser cavity. The name of the method originates from the Q-factor, the quality factor of an optical resonator, which describes the rate of photon loss out of the cavity. In Q-switching the Q-value is first kept low in order to suppress lasing and store energy inside the laser material, and then quickly switched to a high value for rapid onset of lasing. A passive Q-switch operates without any external control relying on the process of saturable absorption. The transmission of a saturable absorber or Q-switch increases as a function of the light intensity. Before the onset of the pulse the saturable absorber is opaque and the

cavity has a low Q. With constant energy feed into the system, the population inversion and the gain of the laser medium increase with time. At some point the laser reaches the low-Q threshold and coherent light starts to build up in the cavity. This bleaches the saturable absorber, quickly reducing the loss in the cavity and increasing the gain of the laser cavity to a very high value. The stored inversion is then released in a giant pulse, after which the saturable absorber starts its recovery for the next cycle [8, 10, 21].

2.1 Laser gain media

Laser operation has been demonstrated in solid, liquid, and gas phases of matter. The solid phase is often preferred due to its high density that allows the required amount of active ions to be incorporated in the smallest volume. The active ions are usually doped in small concentrations into crystals or glasses, although stoichiometric laser materials also do exist [10]. The requirements for the host material are plenty. It should have good mechanical properties, high enough thermal conductivity, it should be available in large enough sizes with good optical quality and transparency, and the particular ion must fit into the crystal lattice without inducing excessive strain. Glasses can be manufactured in very large sizes and doped with high concentrations, but their thermal conductivity is low due the disordered internal structure. Crystalline hosts have much better thermal conductivity, and they are thus preferred in miniature solid-state lasers.

2.1.1 Active ions

Stimulated emission, the fundamental process behind the laser operation, is a photon induced transition (electronic, vibrational, rotational) of an atom or a molecule from a higher energy level to a lower energy level. A useful laser transition must necessarily have a metastable upper state for accumulation of the population inversion, and there has to be an efficient way of exciting atoms onto this level. Particularly well suited for laser operation are the trivalent ions of the rare-earth elements that occupy the periodic table from Cerium (58) to Lutetium (71). The most utilized members of this group are Neodymium, Ytterbium, and Erbium. The laser operation of rare-earth ions is based on electronic transitions in the partially filled 4f-shell [10]. The line widths of the these transitions are exceptionally narrow due to the shielding effect of the outer 5s and 5p electronic shells against the crystal field, giving rise to high gain and long fluorescence

Table 2.1: Physical parameters of laser crystals used in the thesis.

Laser crystal	Nd:YAG[(1)]	Nd:$GdVO_4$[(2)]	Ti:Al_2O_3[(3)]
Emission wavelength	1064.2 nm	1065.4 nm	700–900 nm
	1122.7 nm		
Optical axis	isotropic	c	a
Eff. emission cross section	2.6×10^{-19} cm^2	1.2×10^{-19} cm^2	2.8×10^{-19} cm^2
	2.6×10^{-20} cm^2		
Fluorescence lifetime	230 μs	100 μs	3 μs
Doping	1 %	1%	0.1 %
Thermal conductivity	13 W/mK	8.6 W/mK	33 W/mK
Change of index dn/dT	7.3×10^{-6} K^{-1}	13.8×10^{-6} K^{-1}	13×10^{-6} K^{-1}
Emission linewidth	0.45 nm	1.2 nm	$\sim$180 nm
	1.2 nm		
Pump wavelength	808 nm	808 nm	400–600 nm
Absorption coefficient	$\sim 4\frac{1}{cm}$	$\sim 6\frac{1}{cm}$	$\sim 2.3\frac{1}{cm}$ (c-pol)

[(1)]: [10, 22, 23] [(2)]: [23–27] [(3)]: [10, 28, 29]

lifetimes that allow for efficient storage of energy in the ions for Q-switched operation. Ions of transition metals such as Titanium and Chromium are also popular laser materials. The shielding effect of the outer electronic shells is much weaker in these ions, and hence the laser energy levels are strongly coupled with the crystal fields and lattice vibrations in the host crystal, resulting in short fluorescence lifetimes and broad emission spectra [10].

2.1.2 Host crystals

Two of the most widely used host crystals in lasers are Yttrium-Aluminum-garnet (YAG) and Aluminum-oxide (Sapphire, Ruby). They are both mechanically hard and durable crystals that have high thermal conductivity (for being a dielectric). The first ever laser operation was demonstrated by T. Maiman in Chromium-doped Aluminum-oxide (Ruby) in 1960 [30]. Later on, Aluminum-oxide doped with Titanium or Titanium-sapphire

(Ti^{3+}:Al_2O_3) has become the state-of-the-art laser material of mode-locked oscillators for femto-second pulse generation [29]. The YAG crystal has been doped at least with Ytterbium, Neodymium, and Erbium [31–33]. Nd^{3+}:YAG is a particularly well established laser material due to its long lifetime of the excited state, high emission cross-section at the wavelength of 1064 nm, and excellent thermal and mechanical properties [22].

Some host crystals are birefringent and have anisotropic crystal fields. A single laser transition can then emit light at different wavelengths depending on the orientation of the crystal inside the cavity. For an example, the wavelength of the $^4F_{3/2}(R_2) \rightarrow {}^4I_{3/2}(Y_3)$ transition of the Nd^{3+}-ion is 1064.2 nm in the isotropic YAG crystal, 1063.2 nm in the a-cut $GdVO_4$ crystal, and 1065.4 nm in the c-cut $GdVO_4$ crystal [22, 24]. Table 2.1 lists the physical properties of the laser crystals that have been used for the research summarized in this thesis. The orientations of the crystal axes with respect to the optical axis of the cavity are illustrated in Fig. 2.1.

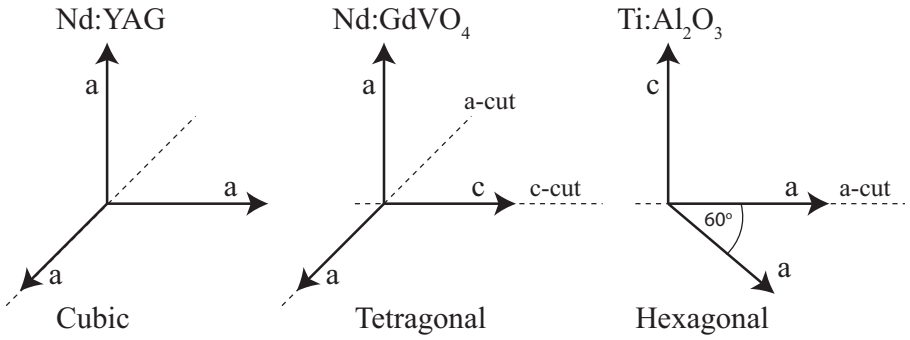

Figure 2.1: Orientation of the crystal axes (a,c) with respect to the optical axis of the cavity (dashed line).

2.1.3 Energy-level structure of Nd:YAG

Nd^{3+}:YAG is a typical laser gain medium with four main energy levels. The energy level scheme of Nd^{3+}:YAG is depicted in more detail in Fig. 2.2. The population inversion is achieved by exciting the Nd^{3+}-ions by optical pumping into the [$^4F_{5/2}$,$^2H_{9/2}$] pump bands, from which they decay non-radiatively into the meta-stable upper laser state $^4F_{3/2}$ that has a fluorescence lifetime of 230 μs [34]. The laser action takes place between the doubly degenerate Stark levels of the upper state $^4F_{3/2}$ and the lower states $^4I_{13/2}$, $^4I_{11/2}$,

and $^4I_{9/2}$. The number of possible transitions is 33 in all, of which 23 four-level configurations terminate at the $^4I_{13/2}$ and $^4I_{11/2}$ states and 10 (quasi) three-level configurations at the $^4I_{9/2}$ ground state [22]. The strongest laser transitions for each of the three lower states have wavelengths of 1318 nm, 1064 nm and 946 nm, respectively. The $^4I_{13/2}$ and $^4I_{11/2}$ terminal states relax by multi-phonon transitions to the ground state. The time constant of the relaxation process has been estimated to be in the range of tens to hundreds of nanoseconds for the $^4I_{11/2}$ state [7]. In publication [I] a relaxation time of 20 ns is estimated based on experimental measurements fitted to a numerical model of the laser operation.

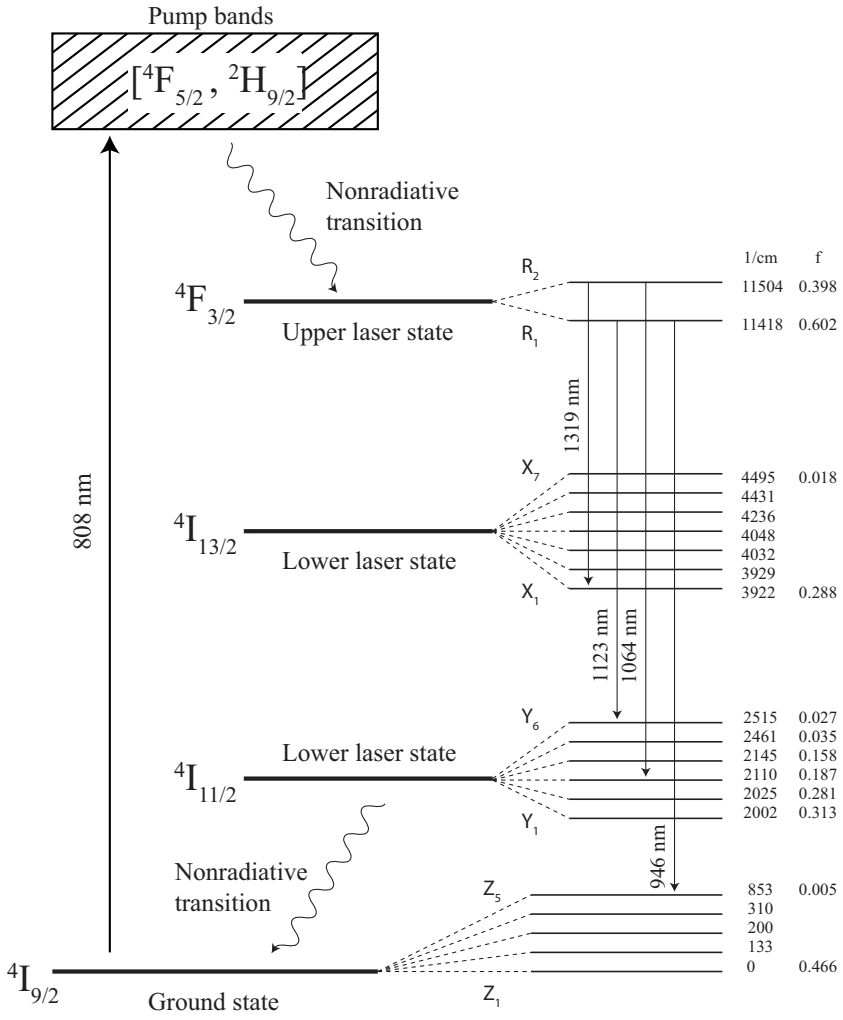

Figure 2.2: Partial energy level diagram of Nd:YAG [22]. The Boltzmann occupation factors f are given at the temperature of 300 K.

In steady-state, the fractional populations of the Stark levels in each state follow the Maxwell-Boltzmann statistics. Perturbations from the steady-state values are dissipated by inelastic phonon collisions, i.e., by a thermalization process. The time-constant of the thermalization is believed to be in the nanosecond to subnanosecond range [7, 35]. The thermalization process among the Stark levels is thus significantly faster than relaxation of the terminal levels to the ground state, implying that it is not necessary to take into account the relaxation of the individual levels when modeling the laser dynamics. The fractional Boltzmann occupation factor of level x is given by

$$f_x = \frac{g_x e^{-E_x/kT}}{\Sigma_x g_{x'} e^{-E'_x/kT}} , \tag{2.1}$$

where g_x is the degeneracy of the level, E_x is the energy of the level, k is the Boltzmann constant, and T is the temperature. The occupation factors of Nd^{3+}:YAG are shown in Fig. 2.2. The fractional occupation factor of the upper laser level, f_a, links together the effective (σ_e) and spectroscopic (σ) emission cross-sections of the laser transition,

$$\sigma_e = f_a \sigma . \tag{2.2}$$

2.2 Laser resonator

The laser resonator provides optical feedback for the process of stimulated emission. In its simplest form it consists of two mirrors that confine light in the space between them. Typically, one of the mirrors is highly reflecting at the laser wavelength, while the other mirror is made partially transparent to let a fraction of the laser light to leak out.

2.2.1 Resonator modes

A laser resonator supports modes, i.e., eigen-distributions and frequencies of light that fulfil the resonance condition, which is the requirement that a round-trip in the cavity does not change the phase and amplitude distribution of the mode. The eigen-distributions of a (hemi)spherical laser cavity are given by the Hermite-Gaussian functions [28, 36]. The photon density $\phi(r)$ of the lowest order mode is symmetric in the radial coordinate r,

$$\phi(r) = \phi(0) \exp\left(-\frac{2r^2}{w^2}\right) , \tag{2.3}$$

where w is the $1/e^2$-radius of the mode. Higher-order Hermite-Gaussian modes are not radially symmetric, but feature maxima and minima separated in orthogonal directions.

However, if this kind of modes are concurrently excited in orthogonal polarization directions, a radially symmetric patter is observed. The spatial extent of the higher-order modes is larger than that of the fundamental mode. Laser operation in only the fundamental mode can be achieved by concentrating the gain at close to the cavity axis. In practice, this is done by end-pumping the laser crystal with a diode laser beam that has a sufficiently small diameter [37].

Each spatial mode has a set of longitudinal resonance wavelengths or frequencies. For the lowest order spatial mode they are calculated by requiring that the optical round-trip length of the cavity is equivalent to an integer multiple m of the wavelength, $2l' = m\lambda$, which gives the resonance frequencies of $\frac{mc}{2l'}$, and a longitudinal mode spacing of $\frac{c}{2l'}$. A typical miniature passively Q-switched laser with an optical cavity length of $l' = 5$ mm has a longitudinal mode spacing of $\frac{c}{2\times 0.005\mathrm{m}} \approx 30$ GHz. Since the gain widths of the laser transitions in a Nd^{3+}-doped crystal are usually larger than 100 GHz [22], it is possible for multiple longitudinal modes to be excited unless the cavity length is shortened to only a few millimeters. In addition to the gain bandwidth and the longitudinal mode separation, the number of excited longitudinal modes depends on the gain in the cavity. A laser typically operates in a single longitudinal mode close to the threshold, but more modes are excited at a higher pump power. Interaction of multiple longitudinal modes by the spatial hole burning effect has the potential to destabilize the output pulse train of a passively Q-switched laser [38, 39]. The pulse train of a passively Q-switched laser is often very stable close to the threshold and becomes progressively more unstable as the pump power is increased.

2.2.2 Geometry

Miniature passively Q-switched lasers make typically use of a flat-flat or hemispherical cavity. A flat-flat cavity is stabilized by the thermal lensing effect taking place in the laser crystal, which has the undesirable side effect of making the mode size dependent on the pump power [10]. The lasers demonstrated in this thesis are realized with the hemispherical cavity that consists of a flat and a spherical mirror facing each other. The geometry of the hemispherical cavity is illustrated in Fig. 2.3. The radius of the beam waist of the lowest order Gaussian mode is on the plane mirror [28]

$$w_0 = \sqrt{\frac{\lambda L_{cav}}{\pi}} \left(\frac{R_c}{L_{cav}} - 1 \right)^{1/4} , \tag{2.4}$$

where λ is the wavelength of the laser radiation, R_c is the radius of curvature of the spherical mirror, and L_{cav} is the length of the cavity. The mode radius inside the cavity

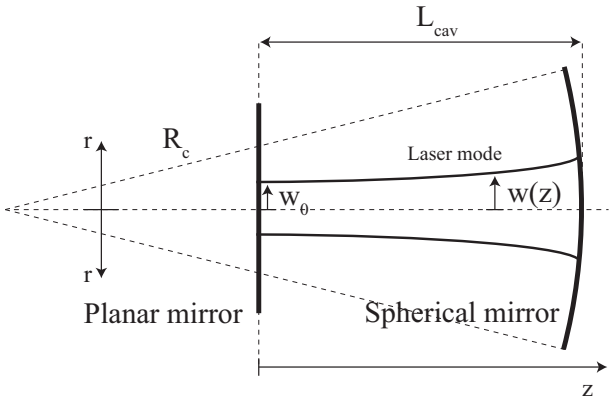

Figure 2.3: The geometry of a hemispherical laser cavity. L_{cav} is the cavity length, R_c is the radius of curvature of the mirror surface, w_0 is the waist radius of the laser beam, and r and z are the radial and longitudinal coordinates, respectively.

is given by

$$w(z) = w_0 \sqrt{1 + \frac{z^2}{z_R^2}}\,, \tag{2.5}$$

where z is the distance from the plane mirror, and z_R is the so-called Rayleigh range of the laser beam [28], i.e., the distance over which the radius of the beam increases by a factor of $\sqrt{2}$. For the lowest order Gaussian beam the Rayleigh range is

$$z_R = \frac{\pi w_0^2}{\lambda}\,, \tag{2.6}$$

which for a hemispherical cavity becomes

$$z_R = L_{cav} \sqrt{\frac{R_c}{L_{cav}} - 1}\,. \tag{2.7}$$

The cavity lengths of miniature passively Q-switched lasers are very short with respect to the radius of curvature of the mirror, $L_{cav} \ll R_c$, so that the Rayleigh range can be approximated as

$$z_R \approx L_{cav} \sqrt{\frac{R_c}{L_{cav}}} \gg L\,. \tag{2.8}$$

In Eq. 2.5 the distance z is always smaller than the cavity length, $z < L_{cav} \ll z_R$, and we can conclude that the mode size inside the cavity $w(z)$ varies only weakly with the

longitudinal coordinate z, and hence we can take $w(z) \approx w_0$. This approximation has been used in [I].

When calculating the properties of the beam outside the cavity, one has to take into account the lensing effect of the spherical output coupling mirror. A concave mirror acts in transmission as a lens with a negative focal length, thus imaging the beam waist to a smaller virtual source and increasing the beam divergence. Beam propagation through an arbitrary paraxial optical system can be conveniently handled by the matrix formalism of paraxial optics [28].

2.2.3 Photon lifetime

An optical resonator has the ability to store light. Due to the losses in the resonator and the fast speed of light, the lifetime of a photon in the cavity is very short but however finite. At a given instant of time, the rate of photon loss is proportional to the number of photons ϕ_N in the cavity,

$$\frac{d\phi_N}{dt} = \gamma\phi_N(t)\,. \tag{2.9}$$

The solution of $\phi_N(t)$ decays exponentially in time,

$$\phi_N(t) = \phi_N(0)e^{-\gamma t} = \phi_N(0)e^{-t/t_c}\,, \tag{2.10}$$

where t_c is the time constant of the decay. The cavity decay time of a miniature passively Q-switched laser resonator is [40]

$$t_c = \frac{t_r}{\ln(1/R) + \ln(1/T_0^2) + L}\,, \tag{2.11}$$

where R is the reflectivity of the output coupling mirror, T_0 is the unsaturated transmission of the Q-switch, L is the round-trip loss, and t_r is the round-trip time of light in the cavity. The round-trip time is calculated as

$$t_r = \frac{2l'}{c}\,, \tag{2.12}$$

where l' is the optical length of the cavity, that is $l' = L + (n-1)l + (n_s - 1)l_s$, where n and n_s are the refractive indices and l and l_s are the length of the laser crystal and the Q-switch, respectively. The definition (2.11) of the cavity decay time follows from the rate-equations for the passively Q-switched laser that are derived in Chapter 3.

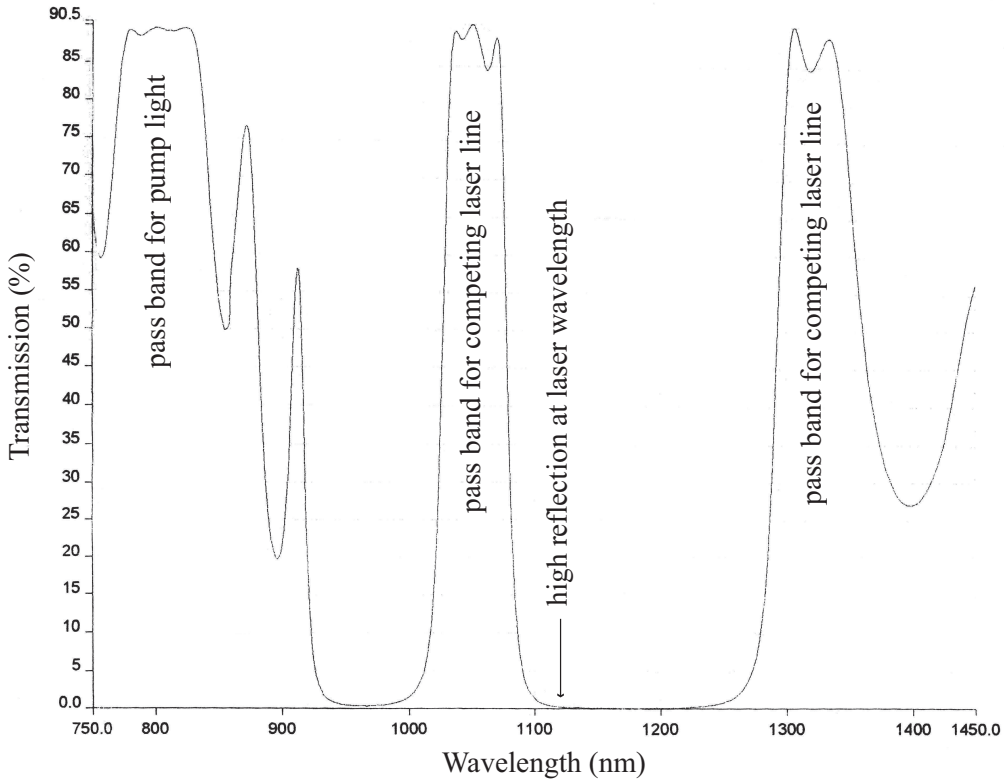

Figure 2.4: Transmission spectrum of the dielectric mirror coating of the Nd:YAG crystal used in [II]. The graph is kindly provided by the crystal manufacturer, Dayoptics Inc.

2.2.4 Optical coatings

Lasers make use of thin-film optical coatings that are deposited on the surfaces on the cavity components. The coatings consist of alternating layers of dielectric materials that have carefully chosen thicknesses and refractive indeces. Interference of reflections originating from the multiple dielectric boundaries gives rise to a strongly wavelength selective transmission spectrum [41]. Thin-film coatings can be used to make surfaces with practically zero transmittivity (high reflection, HR), zero reflectivity (high transmission, HT), or with partial transmission (partially reflecting, PR). Figure 2.4 shows as an example the transmission spectrum of the mirror coating that was deposited on the first surface of the Nd:YAG crystal used in [II]. The surface has high transmission at the pump wavelength of $\lambda_p = 808$ nm, high reflectivity at the laser wavelength of $\lambda_l = 1123$ nm, and high transmission at the competing laser wavelengths of 1064 nm and 1319 nm. The

intra-cavity surfaces of the laser are coated for anti-reflection at the laser wavelength of $\lambda_l = 1123$ nm, and the output coupling mirror surface is coated for partial transmission at the laser wavelength $\lambda_l = 1123$ nm and for high transmission at the competing laser wavelengths of 1064 nm and 1319 nm. The basic scheme of the cavity coatings is illustrated in Fig. 2.5.

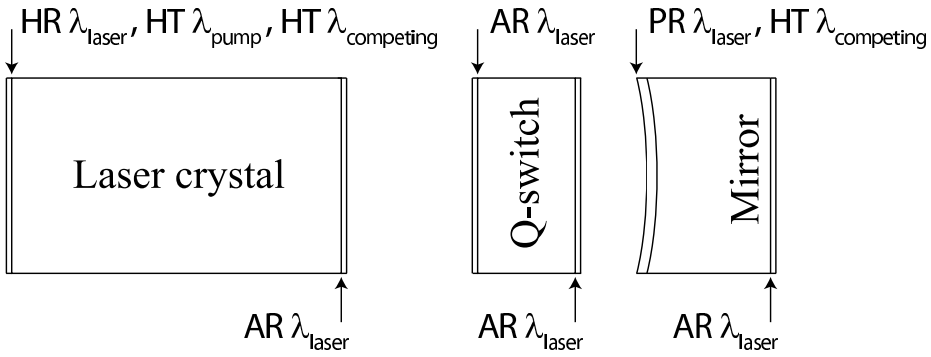

Figure 2.5: Mirror coatings in a typical miniature laser resonator. HR = high reflection, HT = high transmission, AR = anti-reflection, PR = partially reflecting.

2.2.5 Damage threshold

The design of a laser is constrained by physical limitations, one of which is the the light-induced damage threshold of the cavity components. The thin-film optical coatings have generally the lowest damage thresholds, and usually spot-like damages take place on the surfaces of the intra-cavity components. Bulk damage thresholds are generally higher, although there are exceptions such as the grey-tracking damage of the nonlinear KTP-crystal [42,43]. The damage threshold of a dielectric coating is typically ~ 10 J/cm^2 for a pulse length of 1 ns. The threshold scales inversely with the pulse length and the repetition rate, and varies considerably depending on the coating method and quality [44, 45]. The lasers in [I–V] were operated well below the damage threshold, with the exception of the 1123 nm laser demonstrated in [II]. The anti-reflection coating of the saturable absorber crystal was at times damaged during the alignment of the cavity. The damage was spot-like, and small craters were clearly visible in microscope images of the surface. The energy fluence inside the aligned laser cavity was 0.6 J/cm^2 per pulse at a repetition rate

of 12 kHz and a pulse length of 4 ns. Damage during cavity alignment is typical to passively Q-switched lasers, because energy stored in the gain medium can occasionally be released in pulses of much higher fluence than the average.

The damage threshold of the cavity components has to be considered at all steps of the laser design procedure. The numerical models of the laser output may predict the pulse length and energy, but they do not take into account whether the design is physically feasible or not. If the damage threshold is still exceeded at the experimental stage, the pulse fluence can in some cases be reduced below the threshold by active cooling of the laser crystal, which reduces the laser emission cross-section [10] and the pulse fluence. Alternatively, the transmission of the output coupling mirror can be increased in order to reduce the intracavity fluence.

2.3 Creation of population inversion

The laser action requires creation of population inversion by exciting the active atoms or ions to the meta-stable upper laser state. This process is called laser pumping. Lasers in general have been powered with chemical, electronic, and optical pumping, of which the two latter methods are the most common ones. Electronic pumping divides to excitation by electric discharge, as in many gas lasers, and to excitation by injection of current as in laser diodes. The current injection is orders of magnitude more efficient than electric discharge pumping. Crystalline laser media have to be pumped optically, flashlamp being the traditional pump source. However, lamp pumping is inefficient, as a major part of the energy is lost due to the mismatch of the lamp's emission spectrum with the absorption spectrum of the laser medium. The repetition rates of flashlamps are also limited to tens of hertz.

The development of efficient (with $\gtrsim 50\%$ conversion efficiency from electrical to optical energy) and high power diode lasers has opened up the possibility of using them for pumping solid-state lasers [20]. The emission spectrum of diode lasers is narrow enough to match the absorption lines of rare-earth ions, and average powers of multiple watts per emitter are available at infrared wavelengths. The emission wavelength of a diode laser is tuned in a broad scale by the composition (bandgap) of the semiconductor making up the device, and within a few nanometers by adjusting the operating temperature. Lasers based on the Nd^{3+}-ion are pumped by Indium-Gallium-Arsenide (InGaAs) diode lasers operating at wavelengths around $\lambda_p \sim 0.8$ μm. A high brightness InGaAs-diode can emit

3 watts of power from a source area of 1×100 μm^2, corresponding to an intensity of 3 MW per square centimeter.

The emitting facet of a high power diode laser is very asymmetric with an aspect ratio of 50:1 or more. It puts out an elliptical beam of light, whose axes are called the fast and the slow axes according to the amount of divergence in their respective directions. The light along the fast axis originates from the short direction of the emitter. It has good beam quality ($M^2 \gtrsim 1$) and high divergence angle due to diffraction from the narrow aperture. The light along the slow axis originates from the long direction of the emitter. It has worse beam quality ($M^2 \sim 20$), but smaller divergence than the fast axis direction due to the larger dimension of the aperture in this direction. The polarization direction of the diode output is along the slow axis of the beam. The beam of a diode laser is often delivered through an optical fiber in order to shape the diode's elliptical output into a circularly symmetric beam. If the fiber is too short for efficient polarization mixing, the polarization state of the fiber output couples with the mechanical strain on the fiber, which can cause many practical problems. Moving or touching such a fiber can easily affect the polarization state or the absorption efficiency of the laser for which it is used as a pump source. The problem can be circumvented by coupling two indentical laser diodes of orthogonal polarization directions into the same fiber, as it is often done in the laser diode sources of the highest available brightness [41].

The absorption line widths of most rare-earth doped laser crystals are quite narrow [46]. For example, the Nd:YAG laser crystal has an absorption linewidth of $\Delta\lambda \sim 1$ nm centered at $\lambda = 807.5$ nm. The narrow linewidth sets stringent requirements for the wavelength stability of the laser diode, since the diode's output wavelength depends on the junction temperature with a factor of ~ 0.3 nm/K [19, 47]. A temperature control is usually implemented using a thermoelectric cooler with a feedback loop and an electronic controller. The emission wavelength of the laser diode depends also on the injection current, so that the temperature has to be adjusted along with the current if the absorption in the laser crystal is to be maximized. One should also note that the temperature profiles of individual laser diodes vary slightly. An alternative method of wavelength stabilization is to couple the diode's output through a volume Bragg grating [47].

2.3.1 Threshold pump power

A laser must be able to reach the lasing threshold with the available pump source. The figure of merit of a pump source is not only its total output power, but also its brightness. If two laser diodes have identical output powers, the source with the smaller emitter size is brighter and works better for pumping the laser crystal. This is explained by the average pump rate into the laser mode

$$\langle R_p \rangle = \frac{\int_V R_p(r,z)\phi(r,z)\,dV}{\int_V \phi(r,z)\,dV}\,, \tag{2.13}$$

where $R_p(r,z)$ is the spatial distribution of the pump light and $\phi(r,z)$ the distribution of the laser mode given in the cylindrical coordinates [28]. If two laser diodes of equal power but of different emitter size are focused into a spot of equal size, the beam originating from the larger emitter diverges more quickly after and before the focal spot due to its worse beam quality. The value of the overlap integral in the numerator of Eq. (2.13) is consequently smaller for the larger emitter, corresponding to a smaller average pump rate $\langle R_p \rangle$. To make things worse, the fraction of the pump light unaccounted by Eq. (2.13) is not lost, but absorbed outside the volume of the fundamental mode, where it can excite the higher order spatial modes.

If the variation of the pump beam size along the laser axis is neglected, the threshold pump power of a longitudinally pumped passively Q-switched four-level laser is [28, 37]

$$P_{th}(\mathrm{TEM}_{00}) = \frac{\ln\frac{1}{R} + \ln\frac{1}{T_0^2} + L}{2}\frac{h\nu_p}{\xi_a}\frac{\pi(w_l^2 + w_p^2)}{2\tau_f\sigma_e}\,, \tag{2.14}$$

where h is the Planck's constant, ν_p is the frequency of a pump photon, w_p is the $1/e^2$-radius of the pump beam and τ_f is the fluorescence lifetime of the laser crystal. The absorption efficiency ξ_a of the pump light in Eq. (2.14) is given by

$$\xi_a = 1 - e^{-\alpha_p l}\,, \tag{2.15}$$

where α_p is the absorption coefficient of the laser crystal at the pump wavelength, and l is the length of the crystal.

Equation (2.14) shows that low threshold pump power is achieved with a small size of the pump spot and a large product of the fluorescence lifetime and the effective stimulated emission cross-section, $\tau_f\sigma_e$. The size of the pump spot can however not be reduced without a limit, because the thermally induced lensing and aberrations scale inversely

with the size of the pump spot (see Eq. (2.16)) and deteriorate the laser beam quality if too small a pump spot is used.

For example, Eq. (2.14) can be used for calculating the threshold pump power of the 1123 nm laser studied in [II]. The numerical values of the laser parameters are $w_p = 10/8 \times 50$ μm ≈ 65 μm, $w_l = 100$ μm, $R = 0.9$, $T_0 = 0.962$, $L = 0.01$ and $\sigma_e = 2.6 \times 10^{-20}$ cm^2. Substituting the values in Eq. (2.14), we get for the threshold pump power $P_{th} = 0.9$ W$/\xi_a$, while the experimentally obtained value is 0.8 W$/\xi_a$.

2.4 Thermal lensing

A laser releases heat in its operation, when the active ions relax nonradiatively from the pump states to the upper laser state and from the lower laser state to the ground state. The heat flux increases the temperature of the laser crystal and induces local variations in the refractive index of the crystal. This causes a lensing effect, for which a focal length of

$$f = \frac{\pi K_c w_p^2}{P_H (dn/dT)} \tag{2.16}$$

can be derived [10]. In Eq. (2.16), w_p is the radius size of the pump beam, dn/dT is the change of the refractive index with temperature, K_c is the thermal conductivity of the laser crystal, and P_H is the heat load, which is given by the time-averaged difference of the laser input and output powers, $P_H = \langle P_{pump} - P_{out} \rangle_t$. The heat load of a laser can be measured directly, provided the laser has been built, or it can be calculated from the equation

$$P_H = \left(1 - \frac{\lambda_p}{\lambda_l}\right) \xi_a P_{pump} \,, \tag{2.17}$$

where λ_l and λ_p are the laser and pump wavelengths, respectively.

Thermal lensing is often the limiting factor of a laser's output power, because a strong enough lens can destabilize the cavity mode. Also, the thermal lens is not a perfect symmetrical lens, but it has aberrations that can distort the mode profile. The sensitivity of a laser crystal to thermal lensing is often measured with the ratio $(dn/dT)/K_c$. The relative performances of the laser crystals used in this thesis (see Table 2.1) are Ti:Al_2O_3 $\rightarrow 1$, Nd:YAG$\rightarrow 0.7$ and Nd:$GdVO_4$ $\rightarrow 0.25$. The focal length of the thermal lens is thus 4 times shorter for Nd:$GdVO_4$ than it is for Ti:Al_2O_3. This is in accord with the experimental work with the lasers, in which the Nd:$GdVO_4$ crystal was most prone to degradation of the beam quality and saturation of the output power when the pump power was increased.

2.5 Q-switching

Q-switching is a method of generating giant pulses of laser light [21]. The name refers to the Q-factor of the resonator, which is a measure of the resonator's ability to store light. In Q-switching the Q-factor of the cavity is switched between low and high values, or in other words, the loss in the resonator is switched from a high to a low value. The component inducing the loss is called the Q-switch, and it can be driven either actively or passively. In an active Q-switch, fast electronics is required for modulating the loss in a time scale of a few nanoseconds. In a passive Q-switch, the transition is driven by light itself through the process of saturable absorption. Compared to active Q-switching, no electronics is required but the laser is pulsed without external control. The choice of the switch type depends on the application. Passive Q-switches are smaller, simpler and more robust than active Q-switches, but they lack the ability to generate the pulse accurately at a chosen time.

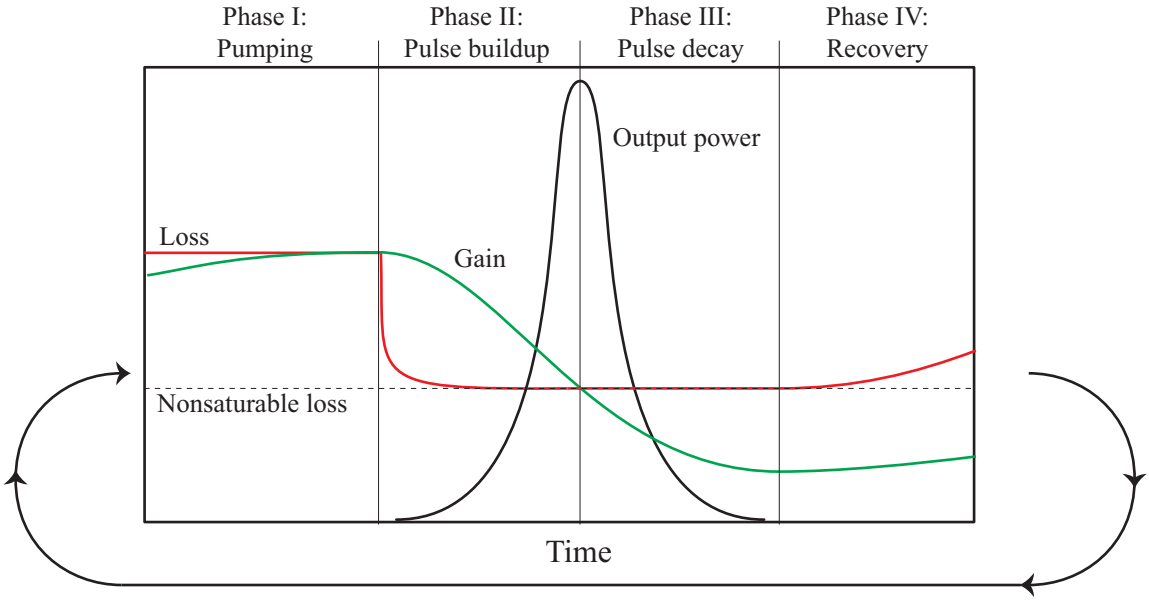

Figure 2.6: Q-switching cycle.

The process of passive Q-switching is illustrated in Fig. (2.6). The repeating cycle can be divided into four phases:

I: The population inversion and gain increase due to the pumping process. At the

onset of the pulse buildup, the gain in the laser crystal reaches the nonsaturated loss level in the resonator.

II: The intracavity intensity builds up by the process of stimulated emission, seeded by a spontaneously emitted photon. The circulating light bleaches the Q-switch and gives rise to a very large net gain due to the accumulated population inversion. The pulse builds up rapidly.

III: The population inversion has been extracted to a level at which the gain equals the saturated loss. The net gain is zero, and the pulse starts to decay. The circulating light extracts more of the population inversion on its way out of the resonator.

IV: The pulse has been extracted and light has left the resonator. The bleached Q-switch relaxes back to its ground-state, increasing the loss back to its nonsaturated value. The population inversion and gain build up for the next cycle.

In an ideal passively Q-switched laser, increasing the pump power would just shorten the pump phase and increase the repetition rate of the laser, while keeping the pulse properties unchanged. In reality, the instabilities of the pulse train increase along with the repetition rate, an at some point the laser output turns chaotic [6].

2.5.1 Saturable absorption in Cr^{4+}:YAG

Passive Q-switches are usually based on the phenomenon of saturable absorption. Probably the most well known saturable absorber or Q-switch is the Chromium^{4+}-doped YAG crystal [48, 49]. Cr^{4+}:YAG shares the excellent thermo-mechanical properties of the Nd^{3+}:YAG laser crystal, and the Cr^{4+}-ion has a very broad absorption band at wavelengths around 1 μm with a relatively high absorption cross-section. The origin of saturable absorption in the Cr^{4+}:YAG crystal stems from the ion's energy level structure, as shown in Fig. 2.7. Absorption from the $^3A_2$ ground-state accumulates population to the meta-stable ^1E excited state, and increases the transparency of the crystal by depleting the ground state population. However, full transparency is not achieved since there is excited state absorption from the ^1E state to higher laying states. The approximate (ground state) absorption spectrum of Cr^{4+}:YAG crystal is shown in Fig. 2.8.

Excluding the reflection losses on the surfaces, the transmission of a Cr^{4+}:YAG crystal is a product of the contributions of the ground state absorption T_{gsa} and the excited state

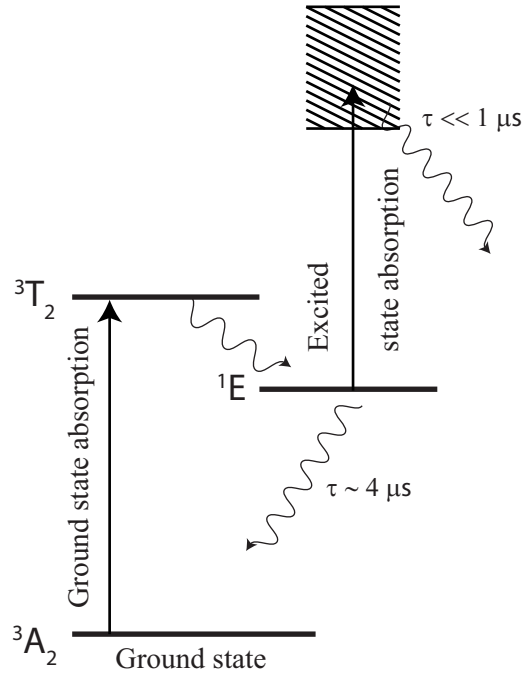

Figure 2.7: Partial energy level diagram of Cr^{4+}:YAG [50].

absorption T_{esa},

$$T_{gsa} = e^{-l_s n_1 \sigma_{gsa}}\,, \tag{2.18}$$

$$T_{esa} = e^{-l_s n_2 \sigma_{esa}}\,, \tag{2.19}$$

$$T = T_{gsa}\, T_{esa} = e^{-l_s (n_1 \sigma_{gsa} + n_s \sigma_{wsa})}\,, \tag{2.20}$$

where n_1 (n_s) and σ_{gsa} (σ_{esa}) are the population density and the absorption cross-section of the ground state (excited state), and l_s is the length of the crystal. The population densities n_1 and n_2 are functions of the saturating intensity. The limiting cases of small intensity (no saturation) and large intensity (full saturation) allow for a simple measurement of the ratio of the absorption cross-sections. At small intensity the entire population is found in the ground state, $n_1 = n_{s0}$, and the unsaturated transmission is

$$T_0 = \exp(-l_s n_{s0} \sigma_{gsa})\,. \tag{2.21}$$

At high intensity all ions are found in the excited state, $n_2 = n_{s0}$, and the saturated transmission is

$$T_{sat} = \exp(-l_s n_{s0} \sigma_{esa})\,. \tag{2.22}$$

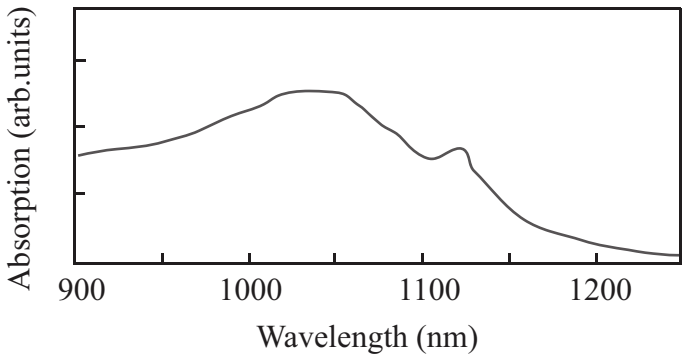

Figure 2.8: Schematic ground state absorption spectrum of Cr^{4+}:YAG crystal [51].

The ratio of the logarithms of the transmission values is

$$\delta = \frac{\ln(T_0)}{\ln(T_{sat})} = \frac{\sigma_{gsa}}{\sigma_{esa}}\,, \tag{2.23}$$

i.e., it is given by the ratio of the absorption cross-sections. The parameter δ is often regarded as the figure-of-merit of a saturable absorber, since it measures the ratio of the useful and nonuseful losses. The δ parameter of a saturable absorber is quite easy to determine experimentally [52]. The unsaturated transmission T_0 is measured with a low intensity continuous-wave beam, whereas the saturated transmission T_{sat} is measured in the focal point of a pulsed beam of sufficient pulse energy. The flux is sufficient when the transmission does not change over an extended depth of focus. One should note that the pulse width of the saturating pulse needs to be in the nanosecond range or longer, since a shorter pulse causes direct excited-state absorption from the $^3T_2$ state, and no saturation of the ground-state absorption is observed [52]. Both T_0 and T_{sat} (and hence δ) are wavelength dependent due to the different spectra of the ground and excited state absorption processes. In [II], the ratio of the absorption cross-sections is measured to be $\sigma_{gsa}/\sigma_{esa} = 3.7 \pm 0.3$ at the wavelength of 1064 nm, in agreement with [48, 52], and a new result of $\sigma_{gsa}/\sigma_{esa} = 5.5 \pm 0.9$ is obtained for the wavelength of 1123 nm.

The exact values of the absorption cross sections have proved to be very difficult to measure. Solved from Eq. (2.18) for low intensities, the ground state absorption cross-section is

$$\sigma_{gsa} = -\frac{\ln T_0}{n_{s0} l_s}\,. \tag{2.24}$$

The problem lies in the unknown density of the active ions, n_{s0}. Chromium ions of different valences can occupy various lattice sites in the YAG crystal, while only the

Cr^{4+} ions at tetrahedral sites give rise to the saturable absorption. The distribution of the ions between the sites and valences is not well known. The reported values of σ_{gsa} for 1064 nm vary by more than one order of magnitude in the range of $0.36 \times 10^{-18} - 7 \times 10^{-18}$ cm^2 [50, 52, 53]. A value of $\sigma_{gsa} \approx 2.7 \times 10^{-18}$ cm^2 is indirectly estimated in [I] by fitting a numerical laser model to the experimental results. The obtained value is in reasonable agreement with the recently published value of $\sigma_{gsa} \approx 1.96 \times 10^{-18}$ cm^2 by Sennaroglu et al. [53].

2.6 Gain-switching

Gain-switching is a method of creating pulsed laser light by varying rapidly the gain in the laser cavity. This is in opposite to Q-switching, in which the cavity loss is varied. The optical gain per unit length is

$$g = \sigma_e n \,, \tag{2.25}$$

where σ_e is the effective emission cross-section of the laser transition and n is the population inversion density. In practice, gain-switching is performed by driving the population inversion quickly to a very high value by pulsed pumping. Gain-switching is used if a certain laser crystal has a desired transition wavelength, but its fluorescence lifetime is too short for efficient storage of energy for Q-switched operation. Typical examples are the laser crystals Ti^{3+}:Al_2O_3 and Cr^{4+}:YAG, which both have a very broad emission bandwidth and a fluorescence lifetime of a few microseconds [54]. The Titanium-sapphire crystal can be pumped with the second-harmonic of the Nd^{3+}:YAG emission at 532 nm, and the Cr^{4+}:YAG crystal directly at the fundamental wavelength of 1064 nm.

2.6.1 Conversion efficiency

The conversion efficiency ξ_g of a gain-switched laser can be estimated by a few simple arguments. By definition, the conversion efficiency is given by the ratio

$$\xi_g = \frac{E_{out}}{E_{pump}} \,, \tag{2.26}$$

where E_{out} and E_{pump} are the energies of the output and pump pulses, respectively. An upper bound for the output energy can be calculated by taking into account the absorption and quantum efficiencies of the pump process, and the residual energy that is left in the

laser crystal in the remaining population inversion. We get

$$E_{out} \leq \xi_a \frac{\lambda_p}{\lambda_l} E_{pump} - E_{res} \,. \tag{2.27}$$

The residual energy is given by the integrated threshold population inversion density multiplied by the energy of a single photon at the laser wavelength,

$$E_{res} = h\nu_l \int n_{th} \, dV \,. \tag{2.28}$$

Assuming a Gaussian intensity distribution for the pump light, the threshold population inversion density of the fundamental Gaussian laser mode is (See Sect. 3.3)

$$n_{th}(r) = \frac{\ln \frac{1}{R} + L}{2l\sigma_e} \left(1 + \frac{w_l^2}{w_p^2}\right) \exp\left(-\frac{2r^2}{w_p^2}\right) \,, \tag{2.29}$$

from which the residual energy follows as

$$E_{res} = h\nu_l \int_0^\infty n_{th}(r) 2\pi r l \, dr = h\nu_l \frac{\ln \frac{1}{R} + L}{2\sigma_e} \left(1 + \frac{w_l^2}{w_p^2}\right) \frac{\pi w_p^2}{2} \,, \tag{2.30}$$

where the longitudinal variation of the mode sizes has been omitted. Combining the above equations we get for the conversion efficiency of a gain-switched laser

$$\xi_g \leq \xi_a \frac{\lambda_p}{\lambda_l} - \frac{hc}{\lambda_l E_{pump}} \frac{\ln \frac{1}{R} + L}{2} \frac{\pi(w_p^2 + w_l^2)}{2\sigma_e} \,. \tag{2.31}$$

Equation (2.31) is in practice an optimistic estimate for the conversion efficiency of an actual laser. In [IV] a gain-switched Ti:Sapphire laser was constructed for the purpose of generating broadband spatially coherent light or supercontinuum light in a microstructured fiber. The energy of the pump pulse is $E_{pump} = 41$ μJ, of which 90% is absorbed by the crystal. The pump and the laser wavelengths are $\lambda_p = 532$ nm and $\lambda_l = 780$ nm, respectively, giving a pump quantum efficiency of $532/780 = 0.68$. The output-coupling mirror of the laser has a reflectivity of $R = 0.9$, and the cavity round-trip loss is estimated to be $L = 0.01$. The waist sizes of the laser and pump modes are $w_l = w_p = 40$ μm. The effective emission cross-section of Ti:Sapphire crystal at 780 nm is $\sigma_e \approx 2.7 \times 10^{-19}$ cm^2 [10]. Using the above values, the residual energy of the laser is $E_{res} = 8.5$ μJ, and the calculated conversion efficiency is $\xi_g = 0.9 \cdot 0.68 - 8.5/41 = 0.40$. The pulse energy and the conversion efficiency of the real laser were found to be $E_{out} = 12$ μJ and $\xi_g = 12/41 = 0.29$, respectively. The achieved conversion efficiency was thus ~ 70% of the theoretical maximum.

2.7 Second-harmonic generation

Most of the efficient solid-state lasers operate at wavelengths outside the visible spectrum, partly because high-power laser diode pump sources are only available for infrared wavelengths. A practical method of obtaining visible wavelengths from infrared lasers is second-harmonic generation (SHG), in which a part of the laser output is converted one octave up in the frequency or half in the wavelength [55]. A Nd:YAG laser emitting at 1064 nm becomes a source of green light at 532 nm. The efficiency of second-harmonic generation depends on the square of the power of the input wave. Thus, high conversion efficiency requires using a resonant cavity for building up the intensity, or high power pulsed light for a single pass pumping through the SHG crystal. A typical conversion efficiency for a pulse with a few kilowatts of peak power is $\gtrsim 30$ % [56, 57].

Second harmonic generation can take place in non-centrosymmetric crystals that experience second-order or $\chi^{(2)}$-nonlinearity. High efficiency of SHG requires matching the phases of the fundamental and the SHG waves along the crystal length, which is achieved by making use of the birefringence of the crystal and choosing the right propagation direction with respect to the crystal axes [11]. Alternatively, some optically nonlinear materials can be quasi-phase matched by periodic poling [58, 59]. The number of available nonlinear crystals is quite limited. They have to be chosen based on requirements on input wavelength, beam quality, and conversion efficiency. Common crystals for SHG of 1064 nm radiation are potassium titanyl phosphate (KTP, $KTiOPO_4$) and lithium triborate (LBO, LiB_3O_5) [60], of which KTP was used in this thesis due to its higher effective nonlinearity. The SHG of 1123 nm light in [II] was achieved by using $KTiOAsO_4$ or KTA, a crystal similar to KTP, due to its better beam quality at 561 nm and higher damage threshold [43, 61]. The phase matching directions of the crystals were calculated by using the SNLO-software package released by Dr. Arlee Smith of Sandia National Laboratories [60].

3 Rate-equation modeling of miniature passively Q-switched lasers

Numerical modeling of passively Q-switched lasers aims at finding a design that produces a desired output in terms of the laser pulse energy E_p, repetition rate f, pulse width Δt, and threshold pump power P_{th}. The models work unfortunately the other way around and the optimum laser design has to be found iteratively. To date, there exists no unified laser theory that would involve all the spatial and temporal aspects of laser emission, but a model has to be developed to the task at hand and its limitations considered. In this thesis the rate-equation approach is used for modeling miniature passively Q-switched lasers [62, 63]. The applicability of the method is improved by developing a normalized geometric model that takes into account the atomic response of the gain medium [7, 40].

A rate-equation description of laser operation includes a temporal model of the processes taking place inside the gain medium and the saturable absorber, and a spatial model of the laser. A common method is to solve the coupled rate-equations for the intra-cavity photon density ϕ, inversion density n, and the ground-state population density of the saturable absorber n_s, and extract the pulse properties from the calculated pulse trail [40, 64, 65]. The spatial dimensions of the equations can vary from a simple point model to the full 3 dimensions. The simplest of the spatial models makes use of plane waves and ignores all spatial inhomogeneities. It is very fast to compute, but potentially inaccurate [62–64]. In a more general geometric model the transverse shapes of the laser mode and the pump beam are explicitly taken into account [40, 64]. This assumption is relaxed in the diffractive model that also solves the dynamic buildup of the resonator mode [65, 66]. The diffractive approach is unfortunately computationally very expensive and hence impractical for optimization of a laser design. In the axial direction the rate-equation models consider only a longitudinally averaged photon density. However, if the round-trip gain of the laser cavity is high, one has to take into account the two-way intensity distribution and the axial variation of the inversion density [8, 9, 67–71]. Solving the traveling wave equations requires a computationally expensive finite-difference method [9, 72].

3.1 Inversion density

Throughout the research contributing to [III–V] it became evident that the existing models for passively Q-switched lasers may not be adequate for describing the kind of lasers with very short cavities that were built. This is due to the simplified energy level scheme of the models, which does not take into account the population dynamics within the laser multiplets of the active ions, but uses a constant inversion reduction factor γ as a proportionality factor of inversion reduction per emitted photon. The factor γ shows in the rate-equation for the inversion density [40, 73]

$$\frac{dn(r,t)}{dt} = -\gamma\sigma c\phi(r,t)n(r,t)\,, \tag{3.1}$$

where it is assigned a value in the range of $f_a \leq \gamma \leq 2$ depending on the rate of the thermalization and relaxation processes of the laser multiplets relative to the cavity decay rate. The lower bound f_a, which is given by the fractional Boltzmann population factor of the upper laser level, is used when the thermalization and relaxation process are much faster than the cavity decay, and the higher bound, respectively, when they are much slower. In addition, there is an intermediate value of $\gamma = f_a + f_b$, where f_b is the fractional Boltzmann population factor of the lower laser level, which applies when the thermalization process is fast and the relaxation process is slow with respect to the cavity decay time [7, 40, 64, 74]. In between these limiting values the dynamics of a passively Q-switched laser is inadequately described by a constant γ parameter, especially so when the ratio between the cross sections of the saturable absorption and the laser emission is small and the bleaching of the Q-switch is slow.

The inversion reduction factor can be calculated dynamically by considering separately the populations densities of the upper and lower laser levels and multiplets, and the thermalization and relaxation processes within them [7]. The schematic model of the energy levels and processes of a four-level gain medium is illustrated in Fig. 3.1. The symbols n_a and n_b mark population densities on the upper and lower laser levels, and n_u and n_l, respectively, on the upper and lower laser level multiplets. The corresponding radially-

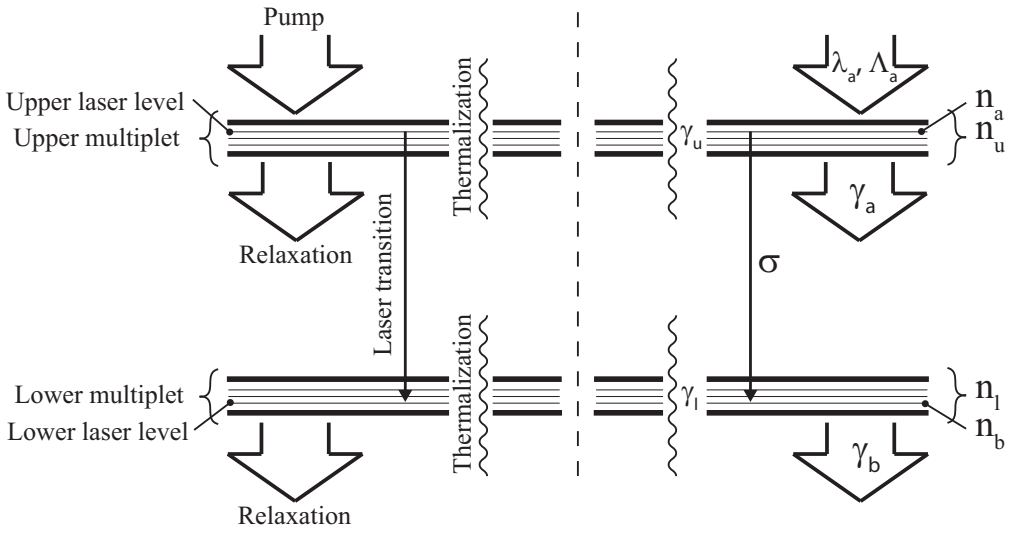

Figure 3.1: Energy level scheme and process model of the laser level multiplets.

dependent rate-equations are

$$\frac{dn_a(r,t)}{dt} = \lambda_a(r,t) - \gamma_u[n_a(r,t) - f_a n_u(r,t)]\,, \tag{3.2}$$
$$- \gamma_a n_a(r,t) - \sigma c\phi(r,t)n(r,t)$$
$$\frac{dn_b(r,t)}{dt} = -\gamma_l[n_b(r,t) - f_b n_l(r,t)] \tag{3.3}$$
$$- \gamma_b n_b(r,t) + \sigma c\phi(r,t)n(r,t)\,,$$
$$\frac{dn_u(r,t)}{dt} = \Lambda_u(r,t) - \gamma_a n_u(r,t) - \sigma c\phi(r,t)n(r,t)\,, \tag{3.4}$$
$$\frac{dn_l(r,t)}{dt} = -\gamma_b n_l(r,t) + \sigma c\phi(r,t)n(r,t)\,. \tag{3.5}$$

In Eqs. (3.2) and (3.4), λ_a and Λ_u are the volumetric pump rates onto the upper laser level and multiplet, respectively, γ_a is the relaxation rate from the upper laser multiplet, γ_u is the thermalization rate within the upper multiplet, and f_a is the equilibrium population fraction of the upper laser level. In Eqs. (3.3) and (3.5), γ_b is the relaxation rate from the lower multiplet, γ_l is the thermalization rate within the lower multiplet, and f_b is the equilibrium population fraction of the lower laser level. The variations of the population densities along the cavity axis have been neglected.

3.2 Saturable absorber

The Cr:YAG saturable absorber is modelled by considering the ground state population density of Cr^{4+} ions, n_s. The population is reduced by absorption to the excited state and replenished by relaxation from the excited state. The rate-equation for n_s is

$$\frac{dn_s(r,t)}{dt} = -\sigma_{gsa} c \phi(r,t) n_s(r,t) + \gamma_s [n_{s0} - n_s(r,t)] \,, \tag{3.6}$$

where γ_s is the relaxation rate from the excited-state and n_{s0} is the unsaturated ground-state population density [35, 40, 63].

The Cr:YAG crystal has a fluorescence lifetime of $\sim$ 3 μs [48, 50]. Since the pulse length of miniature passively Q-switched lasers is a few nanoseconds or very short in comparison to the excited state lifetime, the relaxation of the saturable absorber can be neglected during the release of the Q-switched pulse. Setting $\gamma_s = 0$ in Eq. (3.6) turns it into a homogeneous ordinary differential equation that has the solution [75]

$$n_s(r,t) = n_{s0} \exp\left[-\sigma_{gsa} c \int_0^t \phi(r,t)\, dt \right] . \tag{3.7}$$

Due to the cumulative integration of the photon density, Eq. (3.7) is only valid for calculating a single pulse.

3.3 Photon density

We consider here the longitudinally averaged photon density inside the laser cavity. Photons are added into the laser mode by the process of stimulated emission and removed from the mode by the ground and excited state absorption in the saturable absorber, by absorption, scattering, and diffraction in the laser cavity, and by transmission through the output coupling mirror. A rate-equation for the intra-cavity photon density can be derived by considering one round-trip in the cavity. The laser gain line is assumed to be homogeneously broadened. Starting from an initial photon density of ϕ, after one round-trip the photon density is

$$\phi' = \phi \times R(1 - L_i)^2 e^{2\sigma n l} e^{-2\sigma_{gsa} n_s l_s} e^{-2\sigma_{esa}(n_{s0} - n_s) l_s} \,, \tag{3.8}$$

where R is the reflectivity of the output coupling mirror, l and l_s are the lengths of the laser crystal and the saturable absorber, L_i is the internal one-way loss, and σ, σ_{gsa}, and σ_{esa}

are the cross-sections for the laser emission and the ground and excited state absorption of the saturable absorber, respectively. In Eq. (3.8) the population inversion density is n, the ground state population density of the saturable absorber is n_s, and n_{s0} is its unsaturated value, so that $n_{s0} - n_s$ gives the population density of the excited state. The change of photon density per one round-trip is $\Delta\phi = \phi' - \phi$ or

$$\begin{aligned}\Delta\phi &= [R(1-L_i)^2 e^{2\sigma nl - 2\sigma_{gsa} n_s l_s - 2\sigma_{esa}(n_{s0}-n_s)l_s} - 1]\phi \\ &= [e^{2\sigma nl - 2\sigma_{gsa} n_s l_s - 2\sigma_{esa}(n_{s0}-n_s)l_s - 2\gamma_L} - 1]\phi\,,\end{aligned} \tag{3.9}$$

where we have marked the logarithmic cavity loss by

$$\gamma_L = -\frac{1}{2}\ln R - \ln(1-L_i) \tag{3.10}$$

$$\cong \frac{1}{2}\ln\left(\frac{1}{R}\right) + L_i \tag{3.11}$$

for a small one-way loss $L_i \gtrsim 0$.

If we now assume that the change in the photon density per one round-trip is small,

$$\left|\frac{\Delta\phi}{\phi}\right| \ll 1\,, \tag{3.12}$$

the exponential function in Eq. (3.9) can be estimated with the first two terms of the power series expansion, and we get

$$\Delta\phi = 2\{\sigma nl - \sigma_{gsa} n_s l_s - \sigma_{esa}(n_{s0}-n_s)l_s - \gamma_L\}\phi\,. \tag{3.13}$$

Diving both sides of Eq. (3.13) by the cavity round-trip time $\Delta t = t_r = 2l'/c$ and approximating $\Delta\phi/\Delta t \cong d\phi/dt$ gives the rate-equation for the photon density,

$$\frac{d\phi}{dt} = \frac{2\phi}{t_r}\{\sigma nl - \sigma_{gsa} n_s l_s - \sigma_{esa}(n_{s0}-n_s)l_s - \gamma_L\}\,. \tag{3.14}$$

Finally, to take into account the mode geometry, Eq. (3.14) has to be integrated over the mode area,

$$\int_A \frac{d\phi}{dt}\,dA = \int_A \frac{2\phi}{t_r}\{\sigma nl - \sigma_{gsa} n_s l_s - \sigma_{esa}(n_{s0}-n_s)l_s - \gamma_L\}\,dA\,. \tag{3.15}$$

The output power of the laser is now calculated from the photon density as

$$P(t) = h\nu l' \int_A \left.\frac{d\phi}{dt}\right|_{out} dA = \frac{h\nu l'}{t_r}\ln\left(\frac{1}{R}\right)\int_A \phi(t)\,dA\,. \tag{3.16}$$

The validity of the approximation (3.12) needs some consideration. The 1123 nm laser studied in [II] makes use of a mirror with a reflectivity of $R = 0.9$ and a Q-switch with an initial transmission of $T_0 = 0.96$. Lasers with considerably lower initial transmission ($T_0 < 0.6$) of the switch and lower mirror reflectivity ($R < 0.6$) are easily realized [76], in case of which the approximation (3.12) is no longer valid. Higher order terms should be included in the approximation, or preferably the traveling wave model should be applied [67, 69, 70, 77]. However, it is not clear how big an error the approximation (3.12) introduces in various experimental cases, and further calculations are required.

The rate-equation for the photon density (3.15) can not be used as such, because it lacks the spatial distribution of the photon density. A geometrical shape for the photon density needs to be assumed a-priori. In this thesis, the photon density is assumed to have a Gaussian distribution in the transversal plane,

$$\phi(r,t) = \phi(0,t)e^{-\frac{2r^2}{w_l^2}}\,, \tag{3.17}$$

where w_l is the radius of the laser beam. The integral over the transverse plane in Eq. (3.15) can now be evaluated. Substituting the solution for the saturable absorber from Eq. (3.7) and the form of the photon density from Eq. (3.17) into Eq. (3.15), the rate-equation for the photon density on the cavity axis becomes

$$\begin{aligned}\frac{d\phi(0,t)}{dt} = & \\ & \frac{4}{w_l^2 t_r}\phi(0,t)\int_0^\infty 2\sigma n(r,t) l\, e^{-2r^2/w_l^2}\, r\, dr \\ & - \frac{2(\sigma_{gsa}-\sigma_{esa})n_{s0}l_s\phi(0,t)}{t_r}\frac{1-e^{-\sigma_{gsa}ca(t)}}{\sigma_{gsa}ca(t)} \\ & - \frac{\phi(0,t)}{t_r}\left[\ln\frac{1}{R} + \frac{\sigma_{esa}}{\sigma_{gsa}}\ln\frac{1}{T_0^2} + L\right]\,,\end{aligned} \tag{3.18}$$

where the cumulative photon density is $a(t) = \int_0^t \phi(0,s)\,ds$, the unsaturated transmission of the Q-switch is $T_0 = \exp(-\sigma_{gsa}n_{s0}l_s)$, and L marks the round-trip loss. Equation (3.18) can be used for solving the threshold inversion density $n(r,0)$. Again, a geometrical distribution has to be assumed. In this thesis a Gaussian distribution is used for the inversion density,

$$n(r,0) = n(0,0)e^{-\frac{2r^2}{w_p^2}}\,, \tag{3.19}$$

where w_p is the radius of the pump beam. Substituting Eq. (3.19) into Eq. (3.18) with the condition $d\phi(0,0)/dt = 0$ and solving for the inversion density n gives the on-axis

threshold inversion density

$$n(0,0) = \frac{\ln\frac{1}{R} + \ln\frac{1}{T_0^2} + L}{2\sigma l}\left(1 + \frac{w_l^2}{w_p^2}\right) . \tag{3.20}$$

The presented derivations follow closely those of Zhang et al. [40]. Similar results for top-hat pump beam distribution can be found in [64].

3.4 Normalization of equations

There is not a known analytical solution to the rate-equations (3.15, 3.2–3.6), but they have to be solved numerically. The first step is discretization in which the continuous radial coordinate is turned into a vector of discrete values. The resulting large number of ordinary stiff differential equations is then solved numerically, for example using the solvers in Matlab or any suitable numerical method such as the Adams-Bashforth/Adams-Moulton corrector algorithm [69]. In one run the solution is only obtained for the given values of the input parameters. Since the equations have a large number of parameters, it is laborious and time consuming to span a wider range of their values. Whenever possible, it is practical to reduce the number of variables by normalization, and analyze the contributions of the dimensionless variables [7, 40].

The inversion densities are best normalized ($n_i \rightarrow \eta_i$) to the threshold population density $n(0,0)$, i.e.,

$$\eta_x = n_x / n(0,0) , \tag{3.21}$$

and the time variable ($t \rightarrow \tau$) to the cavity decay time t_c,

$$\tau = \frac{t}{t_c} = \frac{t}{t_r}\left[\ln\frac{1}{R} + \ln\frac{1}{T_0^2} + L\right] . \tag{3.22}$$

The radial coordinate r in Eq. (3.18) is inconvenient to use in numerical integrations because it is unbounded. It can be converted into a bounded variable by introducing a new spatial coordinate

$$y = e^{-2r^2/w_l^2} \, ; r \in [0,\infty[\rightarrow y \in]0,1] . \tag{3.23}$$

The normalized photon density then becomes

$$\Phi(y,\tau) = \sigma c t_c \phi(r(y), t/t_c) , \tag{3.24}$$

where σ is the spectroscopic emission cross-section of the laser transition and c is the speed of light.

Written in the normalized variables, the rate-equations are

$$\begin{aligned}\frac{d\Phi(1,\tau)}{d\tau} &= \left(1+\frac{w_l^2}{w_p^2}\right)\Phi(1,\tau)\int_0^1 \eta(y,\tau)\,dy \\ &\quad -\left(1-\frac{1}{N}\right)\Phi(1,\tau)\frac{1-\exp[-\alpha A(\tau)]}{\alpha A(\tau)} \\ &\quad -\frac{\Phi(1,\tau)}{N}\,,\end{aligned} \tag{3.25}$$

$$\begin{aligned}\frac{d\eta_a(y,\tau)}{d\tau} &= \lambda_a(y,\tau)t_c - \Gamma_u[\eta_a(y,\tau) - f_a\eta_u(y,\tau)] \\ &\quad -\Gamma_a\eta_a(y,\tau) - y\,\Phi(1,\tau)\eta(y,\tau)\,,\end{aligned} \tag{3.26}$$

$$\begin{aligned}\frac{d\eta_b(y,\tau)}{d\tau} &= -\Gamma_l[\eta_b(y,\tau) - f_b\eta_l(y,\tau)] \\ &\quad -\Gamma_b\eta_b(y,\tau) + y\,\Phi(1,\tau)\eta(y,\tau)\,,\end{aligned} \tag{3.27}$$

$$\begin{aligned}\frac{d\eta_u(y,\tau)}{d\tau} &= \Lambda_u(y,\tau)t_c - \Gamma_a\eta_u(y,\tau) \\ &\quad -y\,\Phi(1,\tau)\eta(y,\tau)\,,\end{aligned} \tag{3.28}$$

$$\frac{d\eta_l(y,\tau)}{d\tau} = -\Gamma_b\eta_l(y,\tau) + y\,\Phi(1,\tau)\eta(y,\tau)\,, \tag{3.29}$$

$$\begin{aligned}\frac{dn_{sg}(y,\tau)}{d\tau} &= -\alpha y\,\Phi(1,\tau)n_{sg}(y,\tau) \\ &\quad +\Gamma_s[n_{sg0} - n_{sg}(y,t)]\,,\end{aligned} \tag{3.30}$$

where the normalized relaxation rates are $\Gamma_x = \gamma_x t_c$, the normalized population inversion is $\eta = \eta_a - \eta_b$, and where we have used for the normalized photon density $\Phi(y,\tau) = y\Phi(1,\tau)$ according to Eq. (3.23). In Eq. (3.25), the cumulative integral of the photon density is now $A(\tau) = \int_0^\tau \Phi(y,s)\,ds$, the parameter N is given by [40]

$$N = \frac{\ln\frac{1}{R} + \ln\frac{1}{T_0^2} + L}{\ln\frac{1}{R} + \frac{\sigma_{esa}}{\sigma_{gsa}}\ln\frac{1}{T_0^2} + L}\,, \tag{3.31}$$

and α marks the ratio of the ground-state absorption cross-section of the saturable absorber to the spectroscopic emission cross-section of the laser transition,

$$\alpha = \frac{\sigma_{gsa}}{\sigma}\,. \tag{3.32}$$

Equation (3.30) is only shown for completeness, since it is no longer needed due to the earlier introduction of the solution (3.7) into Eq. (3.15). However, Eq. (3.30) shows

that α sets the saturation rate of the absorber, which turns out to strongly affect the laser dynamics in [I]. It is possible to take into account a mode size difference between the laser crystal and the Q-switch by multiplying α by the ratio of their respective mode areas, A_g/A_s [40].

The initial values of the normalized population densities (3.26–3.29) depend on how the laser pumping is considered. For time-dependent pumping the initial values are zero. On the other hand, the initial values can be written with the aid of the normalized threshold inversion density,

$$\eta(y,0) = y^{(w_l/w_p)^2}\,, \tag{3.33}$$

as

$$\eta_a(y,0) = \eta(y,0)\,, \tag{3.34}$$

$$\eta_b(y,0) = \eta_l(y,0) = 0\,, \tag{3.35}$$

$$\eta_u(y,0) = \frac{\eta(y,0)}{f_a}\,. \tag{3.36}$$

The photon density $\Phi(1,\tau)$ in Eq. (3.25) has to be seeded with a small number of initial photons, mimicking the effect of spontaneous emission in a real laser cavity.

Equations (3.26–3.29) can be reduced into a single integral equation by Fourier transform analysis [7]. Omitting the pump processes after the onset of the Q-switching, we get for the normalized inversion density

$$\eta(y,\tau) = y^{(w_l/w_p)^2} - y\int_0^\tau \gamma(\tau-\tau')\eta(y,\tau')\Phi(1,\tau')\,d\tau'\,, \tag{3.37}$$

where

$$\begin{aligned}\gamma(\tau) =& e^{-\Gamma_a\tau}[f_a + (1-f_a)e^{-\Gamma_u\tau}] \\ &+ e^{-\Gamma_b\tau}[f_b + (1-f_b)e^{-\Gamma_l\tau}]\end{aligned} \tag{3.38}$$

is the inversion reduction factor discussed extensively by Degnen et al. [7]. The original equations are, however, better suited for the necessary numerical calculations.

Combining Eqs. (3.16), (3.17), and (3.24), the instantaneous power $P(t)$ and the pulse energy E are calculated from the on-axis normalized photon density $\Phi(1,\tau)$ as

$$P(t) = \frac{h\nu\,\pi w_l^2}{4\sigma t_c}\ln\left(\frac{1}{R}\right)\Phi(1,t/t_c)\,, \tag{3.39}$$

$$E = \frac{h\nu\,\pi w_l^2}{4\sigma}\ln\left(\frac{1}{R}\right)\int_0^\infty \Phi(1,\tau)\,d\tau\,, \tag{3.40}$$

where h is Planck's constant and ν is the frequency of the laser radiation. Note, that the amount of output coupling is not just $(1-R)\Phi$, but $\ln(1/R)\Phi$ due to the assumption of a small output coupling loss when deriving the rate-equation for the photon density.

3.5 Numerical solution

Solving the rate-equations numerically (3.25 – 3.30) produces the spatial and temporal values of the photon density, the population densities of the laser levels and manifolds, as well as the ground state population density of the saturable absorber. The pulse power and energy are extracted from the photon density using Eqs. (3.39) and (3.40). The

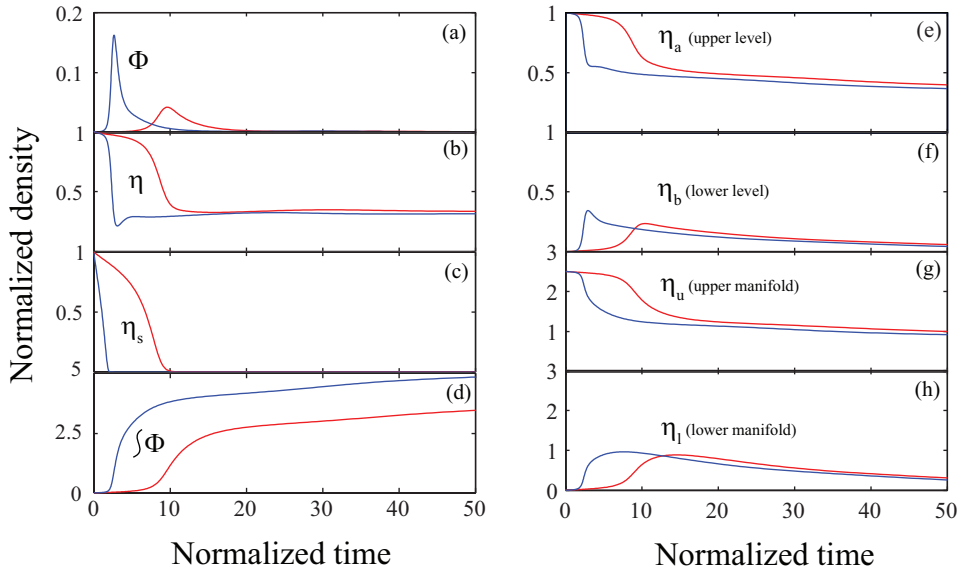

Figure 3.2: Normalized on-axis (a) photon density Φ, (b) inversion density η, (c) saturable absorber ground state population density η_s, (d) integrated photon density $\int \Phi \, d\tau$, and (e-h) population densities of the laser levels and manifolds η_i. The initial inversion is $N = 2.38$ and the pump to laser mode size ratio is $w_p/w_l = 0.92$. The red and blue curves correspond to parameter values of $\alpha = 4.2$ [I] and $\alpha = 42$, respectively. The Boltzmann occupation factors are $f_a = 0.4$ and $f_b = 0.19$. The thermalization and relaxation rates are $\Gamma_u = \Gamma_l = 0.12$ and $\Gamma_a = 0$, $\Gamma_b = \Gamma_u/30$ [I].

pulse width is determined from the pulse trail, and mapped back onto physical time with

Eq. (3.22). There are multiple definitions for the pulse width, of which the full-width at half maximum is used in this thesis. For an example, the red curves in Fig. 3.2 show the calculated on-axis values of the aforementioned quantities for the passively Q-switched 1064 nm Nd:YAG laser discussed in [I]. The accumulation of the population on the lower laser level, the bottle-neck effect, is clearly visible in Fig. 3.2(f). This effect decreases the available population inversion and increases the fall time of the pulse. Also, it can not be reproduced with the models that rely on the use of a constant inversion reduction factor. The blue curves in Fig. 3.2 show the laser behaviour when the ratio of the ground state absorption cross-section of the saturable absorber to the laser emission cross-section (α) is increased tenfold compared to the red curves case. The saturable absorber is bleached quicker, the pulse width is reduced, and the pulse energy is increased. The case is analogous to the difference between the 1064 nm and 1123 nm transitions in Nd:YAG (when the differences in the excited state absorption of Cr:YAG and in the occupation factors of the laser levels are omitted). The order of magnitude lower laser gain at 1123 nm is thus partly compensated by the more efficient Q-switching process. This allows for the construction of the efficient 1123 nm laser demonstrated in [II].

3.6 Parameters

The normalized rate-equation model depends on a large number of parameters, whose effects on the pulse properties are analyzed in detail in [I]. The main parameters of the model are the inversion parameter N, the normalized thermalization rate Γ_t, and the ratio of the ground-state absorption cross-section of the saturable absorber to the laser emission cross-section, α. In addition, the fractional population factors of the upper and lower laser levels f_a and f_b and the relaxation rate of the lower laser level Γ_b play a minor role.

The inversion parameter N, calculated from Eq. (3.31) and appearing in the rate-equation of the photon density (3.25), takes into account the initial transmission T_0 of the Q-switch, the output coupling $1 - R$ and the loss L of the laser cavity, and the ratio of the saturable and nonsaturable losses of the Q-switch through the ratio of the ground and excited state absorption cross-sections $\sigma_{esa}/\sigma_{gsa}$. The value of N is the ratio of the initial inversion density to the high-Q threshold inversion density in the case of $\alpha \to \infty$ [40].

The parameter α is found in Eq. (3.30), where it sets the rate of bleaching of the saturable absorber. The pulse energy and width scale inversely with the value of α. Also, the sensitivity of the pulse width to the relative size of the pump and laser modes increases

considerably with small values of α ($\lesssim 10$). This is the reason why the plane-wave model is not well suited for describing passively Q-switched lasers with a small value of α.

The normalized thermalization rate is the ratio of the cavity decay time to the thermalization time within the laser multiplets, $\Gamma_t = t_c/t_t$. In [I] it is studied how the laser output depends on this parameter. Two different operating regimes are found with respect to the value of α: With a small value, $\alpha \lesssim 10$, the pulse width diverges when the normalized thermalization rate falls below one. With a large value, $\alpha \gtrsim 10$, the pulse width has a maximum when the normalized thermalization rate falls in the range of $0.1 < \Gamma_t < 1$. The pulse energy and peak power scale with the normalized thermalization rate, i.e., the higher the value, the better the laser efficiency.

The pulse energy and the peak power scale inversely with the fractional populations of the laser levels f_a and f_b, so that lower values give better laser efficiency. The contribution of the upper laser level is considerably larger. There is not a general rule for scaling of the pulse length, but it depends on the values of α and Γ_t.

3.7 Comparing numerical and experimental results

A basic problem in comparing the experimental and numerical results is the uncertainty of the input values of the numerical model. The main uncertainty is in the values of the ground state absorption cross-section of the Cr:YAG saturable absorber crystal (see Sect. 2.5.1) and the thermalization time constant of the laser crystal. In this thesis the numerical model is fitted to the experimental results by adjusting these parameters. The obtained values are verified by constructing another laser that makes use of the same crystals and comparing the measured laser output to the calculated laser output. This approach is taken in [I], in which a 1123 nm Nd:YAG laser is used to estimate the thermalization time within the ${}^3F_{3/2} \rightarrow {}^4 I_{11/2}$ transition group of the Nd^{3+} ion in YAG and the ground state absorption cross-section of the Cr:YAG crystal. A 1064 nm Nd:YAG laser is then used for verifying the obtained values.

3.8 Limitations of the model

The presented rate-equation model has been written assuming a spatially uniform gain medium, a small output coupling, a small round-trip gain, a constant mode profile, and

operation in a single longitudinal mode. In addition, the model can only be used for calculating a single output pulse, but not a pulse trail.

The approximation of spatial uniformity is always broken to some extent, because the waste energy of the laser action heats the laser crystal non-uniformly. This induces spatial distributions in the emission cross-section, fractional steady-state populations of the laser levels, and the thermalization and the relaxation rates. The laser operation is likely to be little affected, except in some special cases. The effects are probably observable in lasers that have a slowly bleaching Q-switch, such as the very common combination of a 1064 nm Nd^{3+}:YAG laser crystal and a Cr^{4+}:YAG saturable absorber crystal. In such cases the model works best when calculating the output of a "cold" laser, i.e., when the laser is run at pulsed diode pumping at a low repetition rate and the heating of the laser crystal is minimal.

Small output coupling is assumed due to the approximation $1-R \approx \ln(1/R)$ that is made in deriving the rate-equations. Output couplers with a reflection of $R = 0.9$ do work, but the model can not be expected to work with an output coupler with, e.g, $R = 0.6$. Similarly, if a Q-switch with an initial transmission of $T_0 = 0.6$ is used, the model is likely to fail in some extent. In addition, dynamic transverse-mode distortions may take place in strongly pulsed lasers [78].

The approximation of a single longitudinal mode neglects the effect of spatial hole burning. Spatial hole burning occurs because the population inversion is depleted at the antinodes of the standing electric field inside the laser cavity, and inversion is left at the nodes. In the next Q-switching cycle, an adjacent longitudinal mode can make use of this remaining inversion, giving rise to a periodically alternating pulse train [39, 79]. Again, the model works best for a "cold" laser, as pulsing the laser diode with a period longer than the fluorescence lifetime of the laser crystal wipes out this memory effect. Spatial hole burning can have a very large effect on the laser output. Figure (3.3) shows the measured onset of the pulse train of a Nd^{3+}:YAG laser that is passively Q-switched with Cr^{4+}:YAG saturable absorber crystal and pumped well above the threshold. The model proposed in this thesis can only calculate the first pulse of the train, which is marked in green. The following pulses with alternating sizes can not be predicted because of the assumption of a single longitudinal mode.

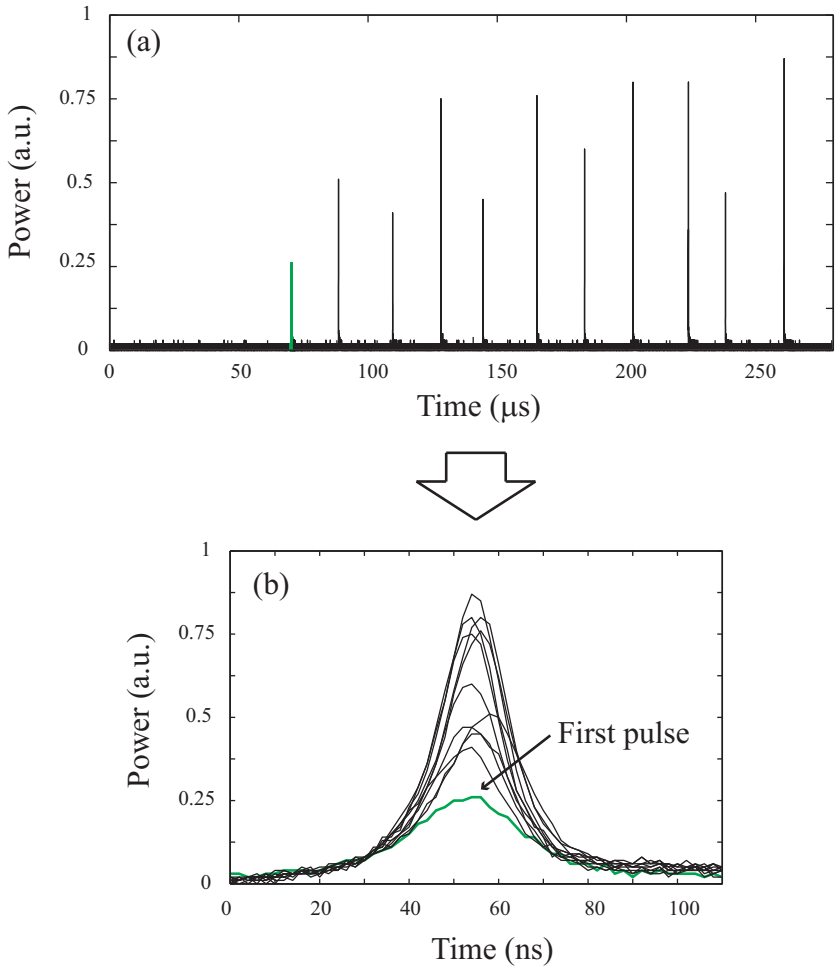

Figure 3.3: (a) Onset of a Q-switched pulse train in a laser with multiple longitudinal modes, when $P_{pump} \gg P_{th}$. (b) Collected pulses.

3.9 Repetition rate

The pulsing frequency or repetition rate f of a passively Q-switched laser can be estimated in multiple ways. One can, for example, solve the rate-equations of the laser in a sufficiently long time period, so that the repetition rate can be obtained from the calculated pulse train. This approach is unfortunately not possible with the model proposed in this thesis. Alternatively, one can calculate the time it takes to obtain the threshold inversion density n_{th} with the pump rate R_p on the laser axis. The result is a higher bound, since the residual inversion of the Q-switching cycle is neglected. A lower bound is obtained by requiring that a fraction of the initial inversion, say a half, is replenished. Taking an

inverse of the pump time, we get for the pulsing frequency a range of

$$\left.\frac{R_p}{n_{th}}\right|_{r=0} \leq f \leq 2\left.\frac{R_p}{n_{th}}\right|_{r=0} . \tag{3.41}$$

The on-axis threshold density of inversion in a Q-switched laser is [40]

$$n_{th}(r=0) = \frac{\ln\frac{1}{R} + \frac{1}{T_0^2} + L}{2l\sigma_e}\left(1 + \frac{w_l^2}{w_p^2}\right) , \tag{3.42}$$

and the on-axis pump rate is [28]

$$R_p(r=0) = \xi_a \frac{P_p}{h\nu_p}\frac{2}{l\pi w_p^2} . \tag{3.43}$$

The 1123 nm laser demonstrated in [II] works at a repetition rate of $f = 12$ kHz when the absorbed pump power is $P_{abs} = 1.6$ W. The pump beam radius is $w_p = 10/8 \times 50$ μm ≈ 65 μm, and the crystal length is $l = 0.3$ cm. According to Eq. (3.43), the on-axis pump rate is $R_p = 3.3 \times 10^{23}$ 1/cm^{3}s. The on-axis threshold inversion density is $n_{th} = 4.2 \times 10^{19}$ 1/cm^3 based on Eq. (3.42), where the substituted values are $R = 0.9$, $T_0 = 0.962$, $L = 0.01$, $\sigma_e = 2.6 \times 10^{-20}$ cm^2, $w_l = 100$ μm, $w_p = 65$ μm, and $l = 0.3$ cm. Using Eq. (3.41), the lower bound of the repetition rate is $3.3/4.2 \times 10^4 \approx 8$ kHz, and the upper bound is respectively 16 kHz. The resulting range of 8 kHz $\leq f \leq 16$ kHz is nicely centered around the measured value of $f = 12$ kHz.

Equation (3.41) neglects the relaxation of the upper laser level, and it is only applicable when the interpulse delay is much shorter than the fluorescence lifetime of the upper laser level or $1/f \ll \tau$. A better estimate for the repetition rate is obtained by considering the simplified rate-equation for the inversion density

$$\frac{dn}{dt} = R_p - \frac{n}{\tau} , \tag{3.44}$$

which has the solution

$$n(t) = R_p\tau(1 - e^{-t/\tau}) . \tag{3.45}$$

The limiting value of $n(t)$ when τ approaches infinity is $\lim_{\tau\to\infty} n(t) = R_p t$. Solving time t from Eq. (3.45) for the threshold inversion density gives

$$t = -\tau \ln\left(1 - \frac{n_{th}}{R_p\tau}\right) , \tag{3.46}$$

the inverse of which gives the lower bound for the repetition rate. Using the same upper bound condition as for Eq. (3.41), the estimated range in which the repetition rate of the laser falls is

$$\frac{-1}{\tau \ln\left(1 - \frac{n_{th}}{R_p\tau}\right)} \leq f \leq \frac{-1}{\tau \ln\left(1 - \frac{n_{th}}{2R_p\tau}\right)} . \tag{3.47}$$

Substituting the values $R_p = 3.3 \times 10^{23}$ 1/cm^{3}s and $n_{th} = 4.2 \times 10^{19}$ 1/cm^3, and the fluorescence lifetime of $\tau = 230$ μs of Nd:YAG, we get an estimate of 5 kHz $\leq f \leq$ 14 kHz for the repetition rate of the 1123 nm laser demonstrated in [II]. The measured value of $f = 12$ kHz fits into the range.

A more accurate estimate of the repetition rate requires knowledge of the residual inversion density n_{res} of the laser crystal. This value can be obtained from the numerical solution of the rate-equations. Solving for the rate-equations, the previously discussed 1123 nm laser has an on-axis residual inversion density of $n_{res} = 0.35\, n_{th}$. Refreshing the inversion back to the threshold value takes a time of

$$t_{refresh} = \frac{R_p}{n_{th} - n_{res}}\,. \tag{3.48}$$

Substituting the numerical values of $R_p = 3.3 \times 10^{23}$ 1/cm^{3}s and $n_{th} = 4.2 \times 10^{19}$ 1/cm^3 gives a refresh time of $t_{refresh} = 83$ μs. The calculated repetition rate is thus $f = 1/(83\,\mu\text{s}) = 12$ kHz, which is exactly the measured value.

4 Microstructured optical fiber

An optical fiber is a dielectric cylindrical object which guides light along its longitudinal axis. Light is confined by total internal reflection into the fiber core that has a higher refractive index than the surrounding fiber cladding. In a conventional optical fiber the refractive index difference between the core and the cladding is obtained by doping the glass. In a microstructured optical fiber the index difference is obtained by filling the cladding partially with air, in the form of an array of thin capillaries running along the length of the fiber [80, 81]. A cladding with a six-fold symmetry, in which the holes are placed in a hexagonal pattern, is the most common. A missing capillary acts as the fiber core. The main structural parameters of the hexagonal cladding are the hole-to-hole distance Λ and the size of the holes d that is often denoted as the relative hole size d/Λ. Values of Λ vary typically in the range of micrometers. A schematic cross-section of the hexagonal microstructured optical fiber is illustrated in Fig. 4.1, and a scanning electron microscope image of a typical fiber cross-section is shown in Fig. 4.2.

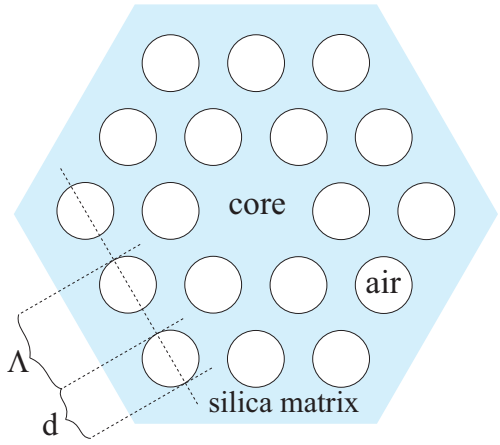

Figure 4.1: Schematic cross-section of a hexagonal microstructured fiber.

The high air-filling fraction of the microstructured cladding gives rise to strong wave guiding effect, and allows for tight confinement of light into a small diameter core. This increases the intensity and the effective nonlinearity in the fiber. The nonlinear coefficient of a fiber is defined as

$$\gamma = \frac{2\pi n_2}{\lambda A_{eff}}\,, \tag{4.1}$$

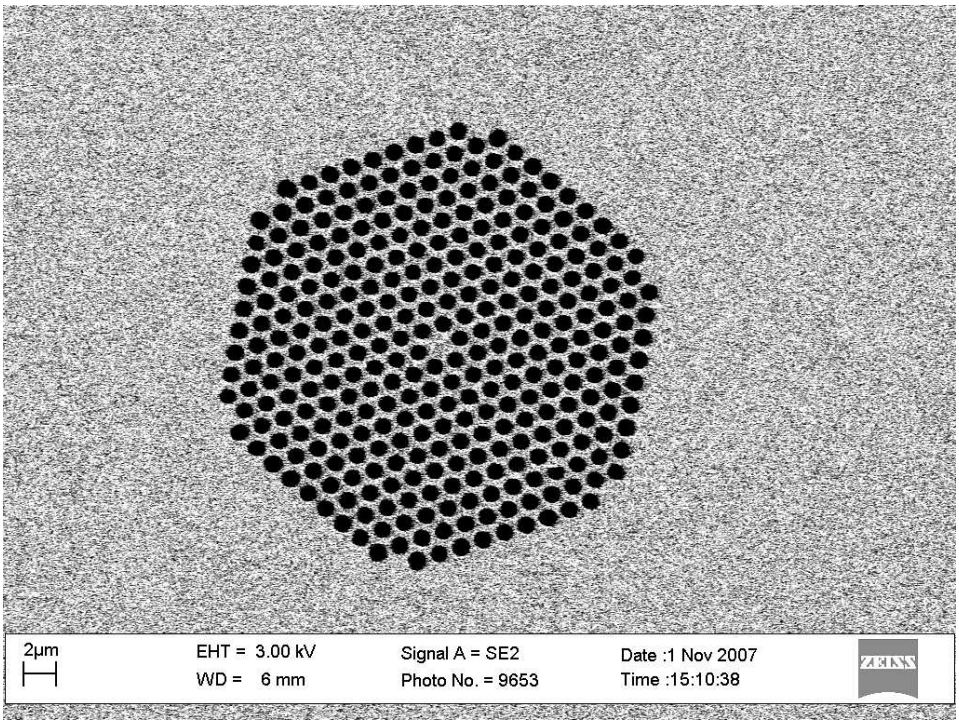

Figure 4.2: A SEM micrograph of a microstructured fiber cross-section.

where n_2 is the Kerr nonlinear coefficient of the medium, λ is the wavelength of the light, and A_{eff} is the effective mode area of the fiber at the given wavelength [82]. A typical single mode fiber for $\lambda = 1064$ nm has a mode field diameter of 5 μm, while values of ~ 1.5 μm can be obtained with a microstructured fiber. In this particular case the gain in nonlinearity is tenfold.

Optical fibers are dispersive like any matter. Light propagates in the fiber at a speed c_m that is smaller than the vacuum speed c. The speed of propagation at a given frequency depends on both the material and waveguide contributions, i.e., on the material and waveguide dispersion. Both of these contributions are taken into account in the effective index of the fiber mode $n_{eff}(\omega) = c/c_m(\omega)$. The phase of light develops through distance z as $\exp[i\beta(\omega)z]$, where $\beta(\omega) = n_{eff}(\omega)\frac{\omega}{c}$ is the propagation constant or wave number of the fiber mode. The speed of the pulse envelope at frequency ω is the group velocity

$$v_g(\omega) = \frac{1}{\beta^{(1)}(\omega)} = \left[\frac{d\beta}{d\omega}\right]^{-1}, \tag{4.2}$$

where $\beta^{(1)} = d\beta/d\omega$ is the group delay that is often used instead of the group velocity. The fiber is said to feature zero group velocity dispersion when the second derivative of the propagation constant with respect to frequency is zero, $d^2\beta/d\omega^2 = 0$. The wavelengths at which this occurs are called the zero dispersion wavelengths λ_{ZDW} of the fiber, and they play a very important role in phase-matching nonlinear optical processes, as is later discussed. Usually, a fiber has one or two zero dispersion wavelengths. The propagation constant and the dispersion of a microstructured optical fiber can be controlled by the geometrical structure of the fiber [83]. The adjustable parameters of the typical hexagonal cladding are the hole pitch Λ and the hole size d. The remarkable property of microstructured optical fiber is its strong waveguide dispersion and the ability to bring the (first) zero dispersion wavelength down to the visible wavelengths from the value of $\lambda_{ZDW} \sim 1.3$ μm of bulk silica fibers [84]. Figure 4.3 shows the dependence of the first zero dispersion wavelength λ_{ZDW} on the fiber pitch Λ and the relative hole-size d/Λ for a range relevant to this thesis. The material dispersion is calculated for silica. The zero dispersion wavelength scales with both the fiber pitch and the relative holesize, since the problem is scale-free apart from the effect of the material dispersion [82].

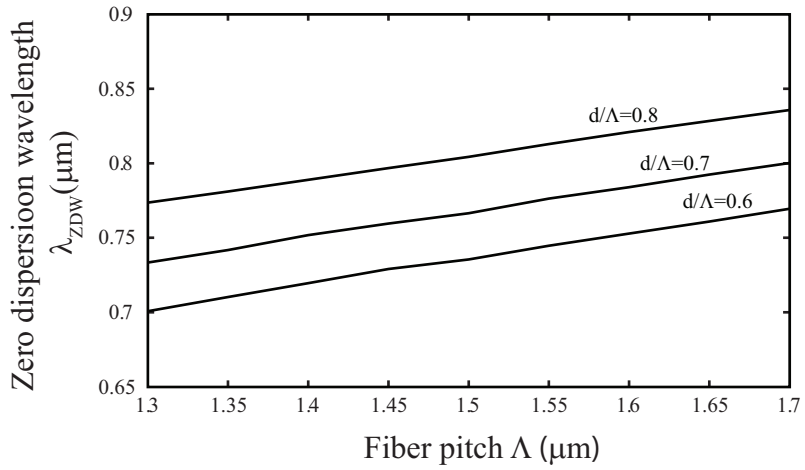

Figure 4.3: First zero-dispersion wavelength λ_{ZDW} of a silica microstructured optical fiber as a function of the fiber pitch Λ and the relative hole size d/Λ. Calculated using the multipole method [85].

The propagation constant of a microstructured fiber is most often slightly polarization dependent due to random variations in the fiber structure [86]. Such a birefringent fiber has two polarization directions that are preserved in transit through the guide. These

eigen-polarization states have slightly different dispersion characteristics, which can affect processes than are sensitive to the phases of the contributing waves. An example of this is the frequency-conversion by four-wave mixing, which in a birefringent fiber generates wavelengths that depend on the polarization direction of the input light [III].

The propagation constant or the effective index of a microstructured fiber has to be evaluated numerically. A variety of numerical models have been developed, of which the multipole method is used in this thesis [83, 87, 88]. One of the main reasons for this choice is the availability of a free implementation, called the CUDOS-utilities software package, which is kindly released to public use by the University of Sydney [85].

The research in [III-V] is conducted with fibers made of fused silica. It is the most exploited material in optical technology due to its low loss and nonlinearity at visible and near-infrared wavelengths, ease of manufacturing, and good mechanical properties. The transmission window of silica is however limited to wavelengths shorter than 2 micrometers. Transmission of longer mid-infrared wavelengths ($\lambda > 2$ μm) requires using fibers made of compound or soft-glasses [89,90]. In ultraviolet wavelengths ($\lambda < 0.3$ μm) silica glass suffers from optically induced damage (solarization) that reduces the transmission of the fiber through the generation of color centers [91, 92]. This can be partly compensated by using silica with high OH-content, however, at the expense of recuded infrared transmission.

The loss spectrum of a typical highly nonlinear microstructured optical fiber used in the thesis work is shown in Fig. 4.4. The general loss level is tens of decibels higher than in conventional telecommunications fibers, because the manufacturing technology of MOFs is yet to develop to the level of bulk silica fibers. Fortunately, only some ten meters of MOF is required for nonlinear frequency conversion of kilowatt peak power pulses, in case of which the fiber loss is not an issue. The main loss mechanism in MOFs is scattering from surface roughness of the air-silica boundaries [93, 94]. Consequently, the loss is highest for fibers with small core diameters and short zero-dispersion wavelengths due to a larger fraction of light propagating in the cladding. The secondary loss mechanism in MOFs is absorption due to the hydroxyl impurities, which gives rise to a strong absorption peak at $\lambda = 1.38$ μm (see Fig. 4.4), easily cutting off a major part of an infrared supercontinuum spectrum [IV]. A dehydrating process has been developed to work out the problem [93]. The fundamental loss floor of glass fibers is limited by the Rayleigh scattering loss, which scales with the fourth power of the optical frequency. For silica glass the Rayleigh loss is ~ 35 dB/km at $\lambda = 0.4$ μm and ~ 1 dB/km at $\lambda = 1$ μm [82].

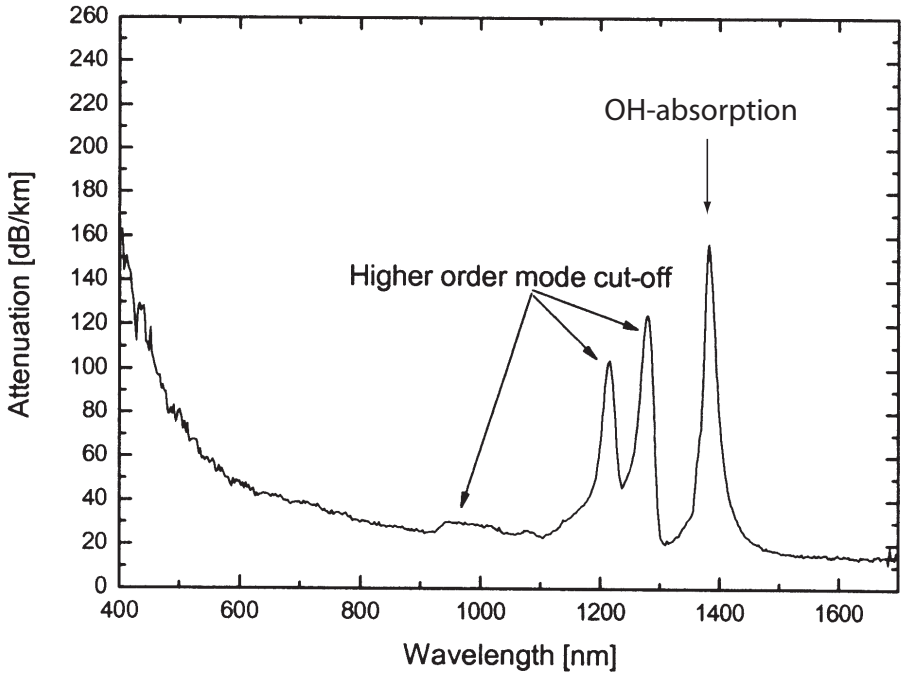

Figure 4.4: Loss spectrum of a typical highly nonlinear MOF used in the thesis work [Crystal Fibre A/S].

5 Nonlinear frequency conversion in microstructured fiber

Miniature passively Q-switched lasers emit light at distinct center wavelengths with a narrow spectral width. If other wavelengths or a broader spectral width are in need, nonlinear frequency conversion in bulk or waveguide media can be applied. Bulk media can have high effective nonlinearities, but the interaction length is quite limited due to the diffraction induced divergence of the beam. In free space the Rayleigh range of a beam with a radius of $w_0 = 30$ μm and a wavelength of $\lambda = 1$ μm is only $z_R \sim 3$ mm. In waveguides such as optical fibers the beam divergence is cancelled, and the effective interaction length is only limited by the waveguide loss. This allows for high effective nonlinearity to be obtained in silica fibers, even if the silica glass has a rather low nonlinear coefficient of $n_2 = 2.2 - 3.4 \times 10^{-20}$ m^2/W [82]. The intensity of light and hence the effective nonlinearity can be increased further in microstructured optical fibers due to the potentially very small mode size, down to a mode radius of $w_0 \lesssim 1$ μm. If a moderate peak power of $P = 1$ kW is coupled into a microstructured optical fiber with a core diameter of 2 μm, the maximum intensity inside the fiber is ~ 30 GW/cm^2. This intensity is of course incident on a given location of the fiber for only a pulse length of a few nanoseconds. In addition to high input intensity, efficient frequency conversion requires matching of the phases of the participating waves. In microstructured optical fibers this can be achieved by controlling the chromatic dispersion by adjusting the geometrical structure of the cladding.

The input light for a nonlinear fiber optical device is typically generated using a pulsed laser. Mode-locked lasers are the traditional workhorses of the field, since they can produce very short pulses ($\Delta t < 1$ ps) at very high repetition rates ($f \gg 10$ MHz) and high peak powers ($P > 10$ kW) [95]. Generation of visible "white laser light" or supercontinuum light in a small-core microstructured optical fiber ($\lambda_{ZDW} = 800$ nm) was first demonstrated by J. Ranka et al. in 2000 by pumping the fiber with a mode-locked Ti:Sapphire laser [12]. The down sides of high-peak power mode-locked lasers are their large physical size, cost, and mechanical complexity. Recently, smaller devices have become available thanks to the introduction of mode-locked fiber lasers. The common Ytterbium-doped fiber laser emits at close to $\lambda = 1$ μm in wavelength [96].

In this thesis the pulsed output of miniature passively Q-switched lasers is converted in frequency in microstructured optical fiber. These lasers have much lower peak power than

mode-locked lasers, but in turn their cavity length is measured in millimeters, and they structure is a lot simpler. The lower peak power is compensated by using longer fiber lengths, because the nanosecond long pulses that miniature passively Q-switched lasers emit are not walk-off limited due to the fiber dispersion as are the subpicosecond pulses of mode-locked lasers [14].

This chapter reviews the nonlinear optical processes relevant to the publications [III-V]. By name they are stimulated Raman scattering, cascaded cross-phase modulation [V], degenerate four-wave mixing [IV], and nondegenerate four-wave mixing [III]. Stimulated Raman scattering is an inelastic scattering process, while the rest originate from the intensity dependence of the refractive index or Kerr effect [82]. Stimulated Raman scattering is not a first-level topic of any of the publications, but it anyhow plays a role in [IV] and [V]. The microstructured optical fibers were obtained from Crystal Fibre A/S. A set of five fibers was drawn from a preform with a relative hole size of $d/\Lambda = 0.7$, the design value of the hole pitch varying from $\Lambda = 1.35$ μm to $\Lambda = 1.55$ μm in 0.05 μm increments. These fibers are known at the manufacturer as the Uranus-fibers. The range of the hole pitch values was chosen to span over the pitch of the fiber that S. C. Buchter et al. used in their dual-wavelength pumped supercontinuum source [97], so that the physics behind the anomalous blue shift of the visible pump could be studied in more detail. The two suspected nonlinear effects were cascaded cross-phase modulation and nondegenerate four-wave mixing, both of which were later observed in these fibers [III,V].

5.1 Stimulated Raman Scattering

Raman scattering is an inelastic scattering process, in which a photon loses a part of its energy and excites a vibrational or a rotational mode in a molecule. If an excited molecule is available, the process can also be reversed. The principle and the schematic spectrum of Raman scattering are shown in Fig. 5.1. The spectral signatures of Raman scattering are the Stokes and anti-Stokes signals that are generated, respectively, at the frequencies ω_s and ω_a,

$$\omega_s = \omega_p - \omega_{21}\,, \tag{5.1}$$

$$\omega_a = \omega_p + \omega_{21}\,, \tag{5.2}$$

where ω_p is the pump frequency and ω_{21} is the frequency of the vibration-rotation mode. Raman scattering can either be spontaneous with spatially isotropic emission, or at high

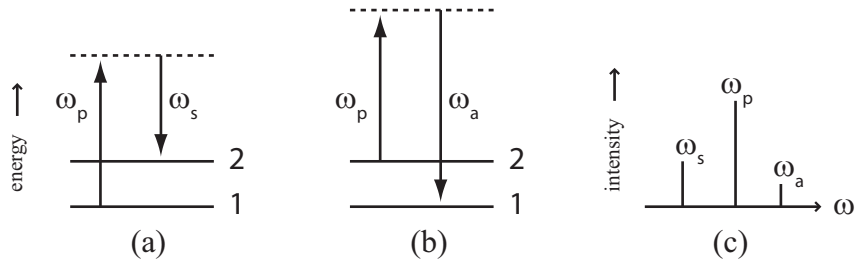

Figure 5.1: (a) Stokes-process of Raman scattering. A molecule is excited via a virtual state. (b) Anti-Stokes process of Raman scattering. An excited molecule gives energy to light field via a virtual state. (c) Frequency spectrum of Raman scattering.

intensities stimulated by the scattering itself with coherent emission. The stimulated scattering process can cascade and give rise to a set of Stokes and anti-Stokes lines, all separated by the same frequency shift. The anti-Stokes process is however much weaker. The higher-order lines have progressively larger bandwidths due to the cascading effect [82].

The Raman gain of silica glass has a peak at $\frac{\omega_p}{2\pi} - 13$ THz and a bandwidth of $\lesssim 40$ THz. The broadness of gain stems from the amorphous structure of glass, which spreads the vibrational frequencies of individual molecules into continuous bands. The Raman gain scales inversely with the pump wavelength [98]. Figure 5.2a shows as an example a Raman spectrum created by pumping a silica fiber at the wavelength of $\lambda_p = 532$ nm.

Stimulated Raman scattering is the dominating nonlinear process when the pump wave propagates in a region of normal dispersion far away from the zero-dispersion wavelengths of the fiber. In the region of anomalous dispersion, Raman gain couples with the modulation instability effect (see Sect. 5.3). Separate Raman peaks do not develop, but the spectrum is smoothly red-shifted due to soliton self-frequency shift [14, 99]. This is illustrated in Fig. 5.2b, which shows the output spectrum of a microstructured silica fiber when pumped in the region of anomalous dispersion at the wavelength of $\lambda_p = 1064$ nm. Stimulated Raman scattering can also be suppressed in the region of normal dispersion, if a second wave is propagated in the region of anomalous dispersion with a similar group-velocity. The effect is due to cross-phase modulation induced modulation instability [V], [14, 82].

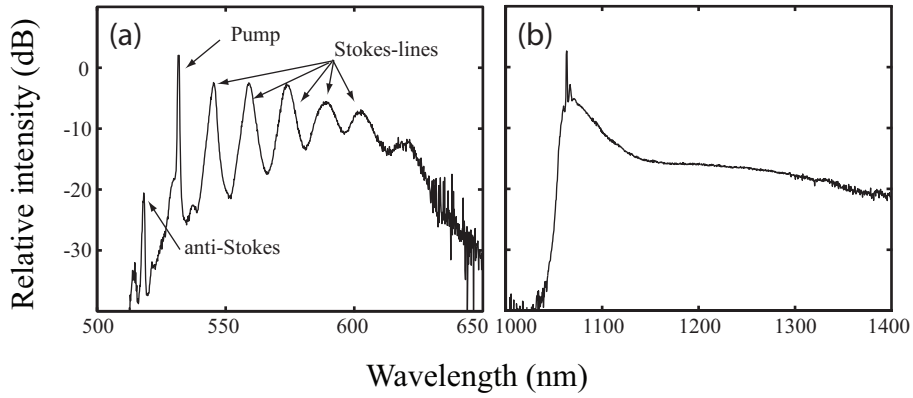

Figure 5.2: Measured spectra of stimulated Raman scattering in (a) normal dispersion and (b) anomalous dispersion region of a microstructured silica fiber. The respective pump wavelengths are (a) $\lambda_p = 532$ nm and (b) $\lambda_p = 1064$ nm. Raman peaks are not observed in (b) because the stimulated Raman effect couples to the process of modulation instability.

5.2 Cascaded cross-phase modulation

Cascaded cross-phase modulation can be used for inducing large blue- and red-shifts on a visible pump wave by co-propagating it with an infrared pump wave [14]. This dual-wavelength pumping scheme allows for generation of broadband blue light in a microstructured optical fiber by using a simple passively Q-switched and frequency doubled Nd:YAG laser emitting at $\lambda_{p1} = 532$ nm (green) and $\lambda_{p2} = 1064$ nm (infrared) as the pump source [97]. The first numerical studies on the subject were conducted in 2005 by G. Genty et al., who considered dual-wavelength femtosecond pulses with their wavelengths centered around the first zero-dispersion wavelength of the fiber [100]. Their numerical findings were soon experimentally confirmed by Schreiber et al. [101]. Although femtosecond laser pulses are $\gtrsim 10^4$ times shorter than the nanosecond pulses generated by passively Q-switched lasers, similar spectral broadening of dual-wavelength pulses is observed in microstructured optical fiber. This is explained by the fact that a nanosecond pulse propagating in the region of anomalous region is break down by the modulation instability effect (see Sect. 5.3), which in effect produces a large number of subpulses whose widths are in the femtosecond timescale [14].

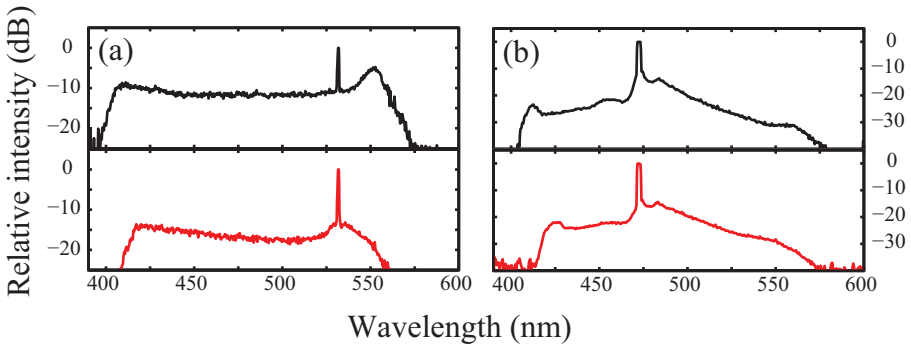

Figure 5.3: Measured spectra in two microstructured fibers (red and black) by using dual-wavelength nanosecond pumping at (a) 532/1064 nm and (b) 473/946 nm. The power of the visible pump is below the threshold of stimulated Raman scattering. The design values of the fiber parameters are $\Lambda = 1.55$ μm (black), $\Lambda = 1.35$ μm (red), and $d/\Lambda = 0.7$ in both. The fibers are 20 m long [V].

Let us next consider in more detail the case in which two pump pulses ($\lambda_{p1} < \lambda_{p2}$) propagate together in a microstructured fiber, one deep in the region of normal dispersion and the other deep in the region of anomalous dispersion. The pulse of the shorter wavelength λ_{p1} is initially stable, as it experiences normal dispersion. The pulse of the longer wavelength λ_{p2} is unstable due to the modulation instability effect, and it breaks into a large number of solitons. The solitons have a very short temporal pulse width, and hence a large frequency bandwidth, which overlaps with the Raman gain bandwidth of silica. This causes an effect called soliton self-frequency shift (SSFS), which shifts the center wavelength of a soliton towards the red wavelengths when it propagates along the fiber [14, 99]. The large number of the solitons produces collectively a smooth continuum spectrum of light, an example of which can be seen in Fig. 5.2b.

The high peak power of the solitons at infrared wavelengths ($\lambda > \lambda_{p2}$) induces a local change in the refractive index of silica through the Kerr-effect, which in turn affects the phase of the co-propagating visible pulse (λ_{p1}). This process is called cross-phase modulation (XPM) [82]. As the phase of the visible pulse is being modulated, its spectrum broadens and the pulse envelope is strongly distorted. The created subpulses have short temporal width, and hence a large frequency bandwidth. XPM induced spectral broadening can cascade, if spatial overlap of the infrared solitons and the visible subpulses is maintained along the length of the fiber. The infrared and the visible frequency compo-

nents must necessarily have similar group velocities. This can be achieved by making use of the strong waveguide dispersion of microstructured optical fiber. In publication [V] it is experimentally studied how the group-delay profile of the fiber affects the extent of the XPM-induced spectral broadening.

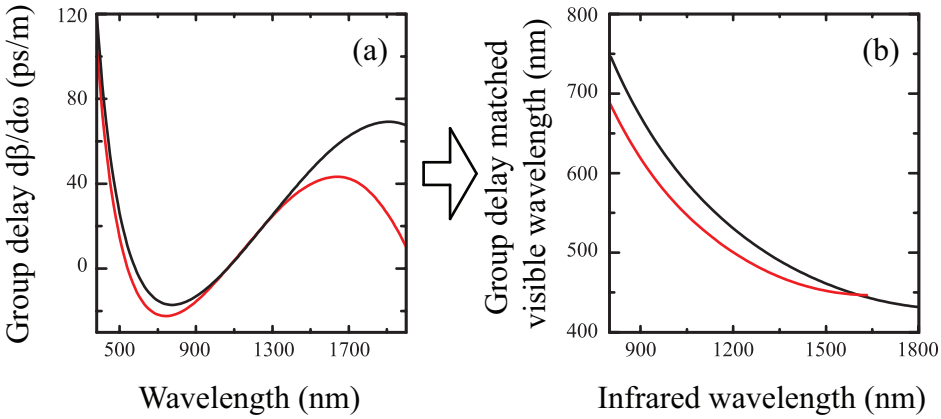

Figure 5.4: Calculated group delay (a) and group delay matching (b) curves for microstructured optical fibers with pitches of $\Lambda = 1.55$ μm (black) and $\Lambda = 1.35$ μm (red). The relative hole size is $d/\Lambda = 0.7$ [I].

The output spectra of two microstructured fibers with 532/1064 nm and 473/946 nm dual-wavelength pumping are shown in Fig. 5.3. The cutoff wavelengths of the spectra are seen to be quite independent of the locations of the pump wavelengths, especially on the blue side, which indicates that the location of the cutoff is a property of the fiber. The calculated group delay profiles of the studied fibers are shown in Fig. 5.4a, together with the group delay matching between the visible and the infrared wavelengths in Fig. 5.4b. The visible continuum is expected to cover all the wavelengths, for which there is an excited infrared wavelength with an equal group delay. The required broad infrared spectrum is easily generated from the longer pump wavelength by the combination of modulation instability and SRS (See Fig. 5.2b.) The group-delay of the shortest generated visible wavelength is equal to the maximum group-delay found in the infrared spectrum, which for a fully developed infrared spectrum is found at the second zero dispersion wavelength of the fiber. Respectively, the maximum red-shift of the shorter wavelength pump is set by the minimum group-delay of the infrared spectrum, which often corresponds to that of the infrared pump wavelength. The case is illustrated in Fig. 5.5 by showing the group delay matching diagram together with the experimental spectra. There is a qualitative agree-

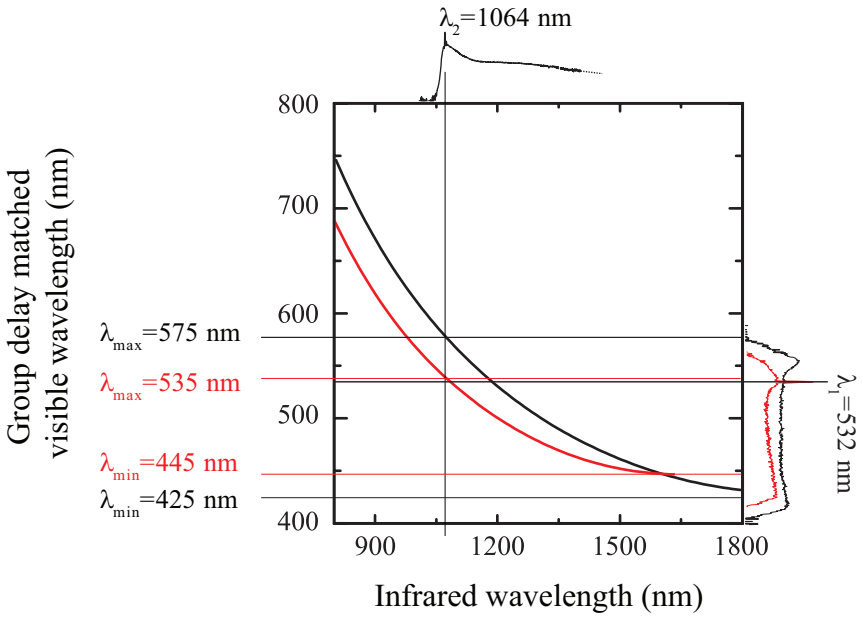

Figure 5.5: Relation of the measured XPM-spectrum to the calculated group delay matching curve of the fibers. The spectra are from Figs. 5.3 and 5.2(b), and the black and red curves correspond to Fig. 5.4.

ment between the extent of the experimental spectra and the calculated group-velocity-matched wavelength region. The discrepancy is accounted for the fact that the design parameters of the fibers were used in the calculations, while the actual fiber parameters are likely to be slightly different.

Figure 5.6 shows the evolution of the visible and infrared spectra for increasing input power. The power of the visible pump pulse is at all times kept below the threshold of stimulated Raman scattering. It is clearly seen that the redshift of the infrared continuum induces a blueshift of the visible pump pulse. The spectrum of the visible pulse does not broaden if the co-propagating infrared pulse is absent or it has low power.

5.3 Degenerate four-wave mixing

Four-wave mixing (FWM) is a third-order optical nonlinear process that arises from the $\chi^{(3)}$-nonlinearity of matter, the leading type of nonlinearity in centrosymmetric medium such as glass. Four-wave mixing is a parametric process in which no net energy exchange

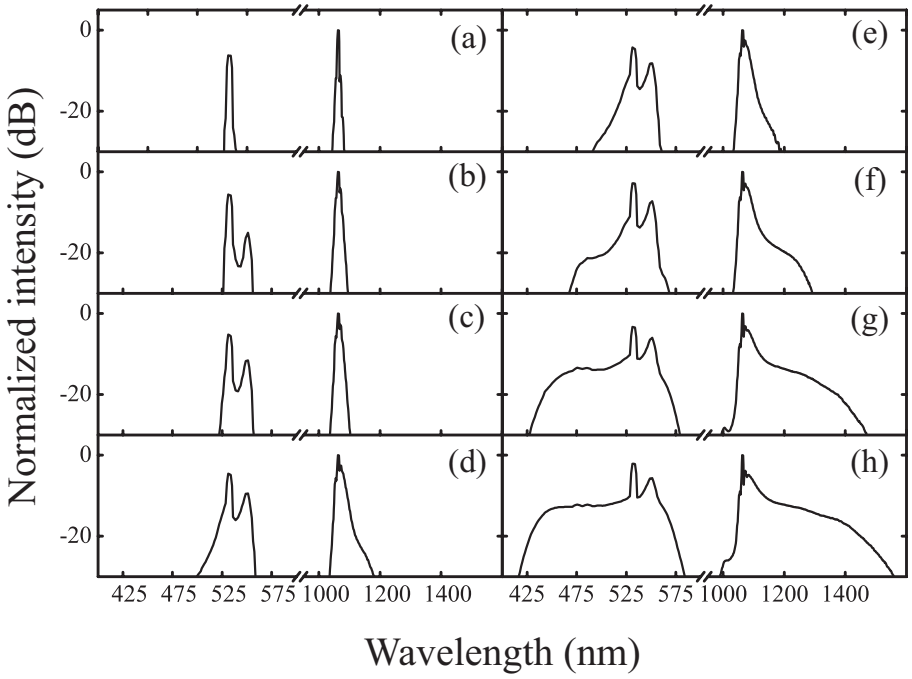

Figure 5.6: Measured evolution of spectrum when nanosecond dual-wavelength 532/1064 nm pump pulses of increasing power (a→h) are coupled into a microstructured fiber with the design values of $\Lambda = 1.55$ μm and $d/\Lambda = 0.7$ [V].

occurs between the medium and the participating waves. In degenerate four-wave mixing process two pump photons of equal frequency (ω_p) are annihilated and two new photons at frequencies ω_s and ω_i, called signal (s) and idler (i), are created. Conservation of both energy and momentum is required. The frequencies of the photons satisfy the condition

$$2\omega_p = \omega_s + \omega_i \,, \tag{5.3}$$

and the corresponding propagation constants satisfy the phase-matching condition [82]

$$2\beta_p = \beta_s + \beta_i \,. \tag{5.4}$$

The phase-matching condition has also a power dependent contribution. In the approximation of undeplepted pump waves a term of γP, where γ is the effective nonlinearity of the fiber and P is the total power of the pump waves, is added on the right-hand side of Eq. (5.4). The principle and a schematic spectrum of degenerate four-wave mixing are illustrated in Fig. 5.7.

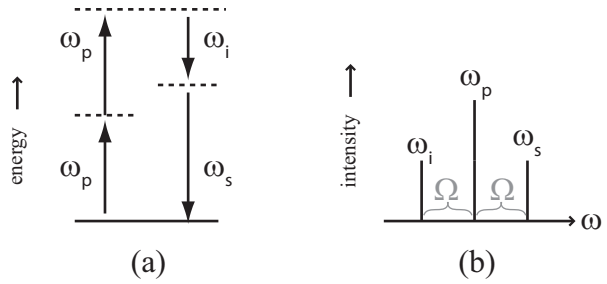

Figure 5.7: Principle (a) and schematic frequency spectrum (b) of degenerate four-wave mixing process.

Degenerate FWM is widely exploited for nonlinear frequency conversion in optical fiber [102, 103], because it is easily phase-matched by pumping the fiber at close to its zero-dispersion wavelength. This follows from Eq. (5.4) by substituting the propagation constants $\beta_{s,i}$ with their Taylor series expansions around the pump frequency ω_p,

$$\beta_{s,i} = \beta_p + \left.\frac{d\beta}{d\omega}\right|_{\omega=\omega_p} (\omega_{s,i} - \omega_p) + \frac{1}{2} \left.\frac{d^2\beta}{d\omega^2}\right|_{\omega=\omega_p} (\omega_{s,i} - \omega_p)^2 + \cdots , \tag{5.5}$$

and taking into account the fact that the signal and idler frequencies are situated symmetrically around the pump frequency,

$$\omega_p - \omega_i = \omega_s - \omega_p = \Omega \, . \tag{5.6}$$

Dropping the higher order terms of Eq. (5.4), we get

$$\left.\frac{d^2\beta}{d\omega^2}\right|_{\omega_p} \Omega^2 = -\frac{2\pi c}{\omega^2} D\Omega^2 = 0 \, , \tag{5.7}$$

where the dispersion D is defined as [82]

$$D = -\frac{2\pi c}{\lambda^2} \left.\frac{d^2\beta}{d\omega^2}\right|_{\omega=\omega_p} = -\frac{\omega^2}{2\pi c} \left.\frac{d^2\beta}{d\omega^2}\right|_{\omega=\omega_p} . \tag{5.8}$$

Degenerate four-wave mixing is thus phase-matched when the fiber dispersion is zero at the pump wavelength. Once the propagation constant of a fiber is measured or calculated as a function of frequency, Eqs. (5.3) and (5.4) can be used for calculating a phase-matching diagram that shows the wavelengths of the signal and idler waves as a function of the pump wavelength. Best numerical accuracy is achieved by doing all the

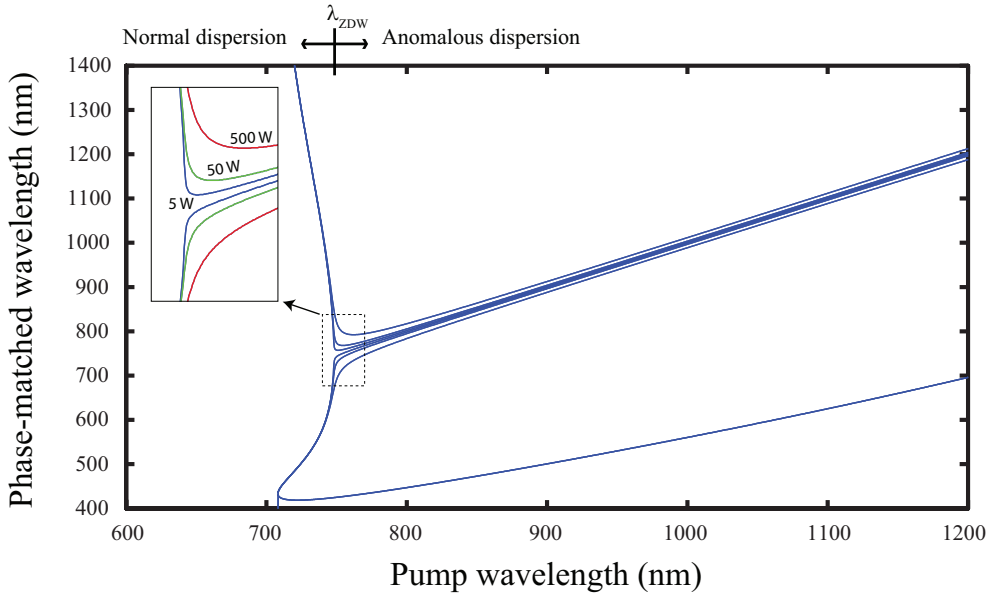

Figure 5.8: Calculated phase-matching diagram of degenerate four-wave mixing for the microstructured optical fiber used in [IV]. The fiber pitch and the relative hole size are measured to be $\Lambda = 1.47$ μm and $d/\Lambda = 0.74$ (older less accurate values of $\Lambda = 1.48$ μm and $d/\Lambda = 0.7$ are used in the publication). A value of $\gamma = 50$ $\frac{1}{\mathrm{W\,km}}$ is used for the nonlinearity of the fiber.

calculations in the frequency domain, and using the wavelength domain only for illustration.

Figure 5.8 shows the calculated phase-matching diagram of the fiber used in [IV]. The contribution of the pump power has been taken into account in the approximation of an undeplepted pump wave. The values in the phase-matching diagram are specific to the fiber, put the shape is general. Two kinds of solutions are found. In the region of normal dispersion ($\lambda < \lambda_{ZDW} \approx 750$ nm), the signal and the idler wavelengths are widely separated and very sensitive to the value of the pump wavelength. In the region of anomalous dispersion ($\lambda > \lambda_{ZDW} \approx 750$ nm) the signal and the idler are closely spaced and more sensitive to the pump power. In the latter case the degenerate four-wave mixing is often called modulation instability, because the appearance of the sidebands in the frequency domain corresponds to modulation of the pulse shape in the time domain. Since the sidebands are closely spaced with the pump wavelength, the modulation instability can cascade and break the pulse into very short soliton pulses. Soliton is the only

stable pulse form in the region of anomalous dispersion [82]. Figure 5.9 shows experimentally measured spectra of modulation instability and degenerate four-wave mixing in microstructured optical fiber.

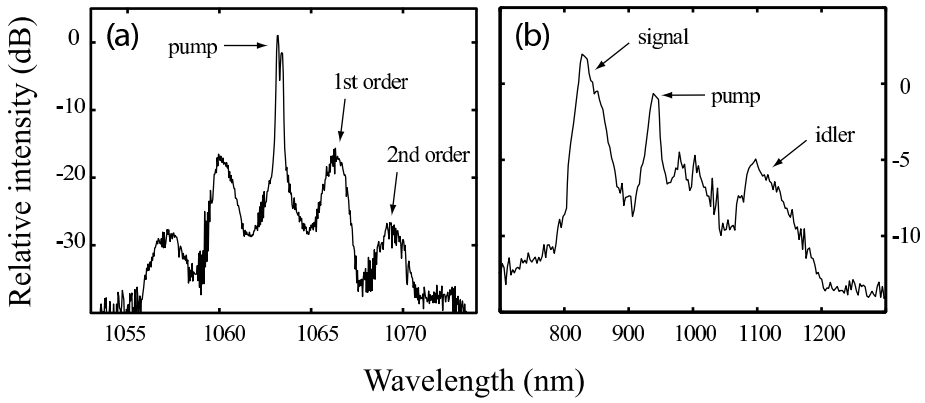

Figure 5.9: (a) Modulation instability sidebands of a $\lambda_p = 1064$ nm pump wave propagating in the region of anomalous dispersion of a microstuctured fiber. (b) Four-wave mixing bands of a $\lambda_p = 946$ nm pump wave propagating in the region of normal dispersion at close to the zero dispersion wavelength.

Degenerate four-wave mixing can be used for generating extremely broadband light or supercontinuum light, if a fiber is pumped in the region of anomalous dispersion at close to the zero dispersion wavelength ($\lambda_p \lesssim \lambda_{ZDW}$). This allows for cascaded FWM to take place, followed by a complex cascade of other nonlinear processes [14, 103]. In [II] we demonstrate a compact broadband source of visible light by pumping a microstuctured fiber with a miniature gain-switched Titanium:sapphire laser. The pump wavelength is $\lambda_p = 780$ nm, and the zero dispersion wavelength of the fiber is estimated to be $\lambda_{ZDW} \approx 750$ nm. One can now compare the obtained spectrum, shown in Fig. 5.10, to the calculated phase-matching diagram of the fiber presented in Fig. 5.8. The spectrum extends down to $\lambda = 420$ nm in accord with the shortest phase-matched wavelength in the diagram.

The bandwidth of the FWM gain depends on the frequency separation of the signal and idler waves from the pump frequency. As a rule of thumb, the larger the separation is, the narrower the bandwidth becomes [82]. This can also be seen from the phase-matching diagram, Fig. 5.8, in which the effect of pump power is very small for large wavelength shifts.

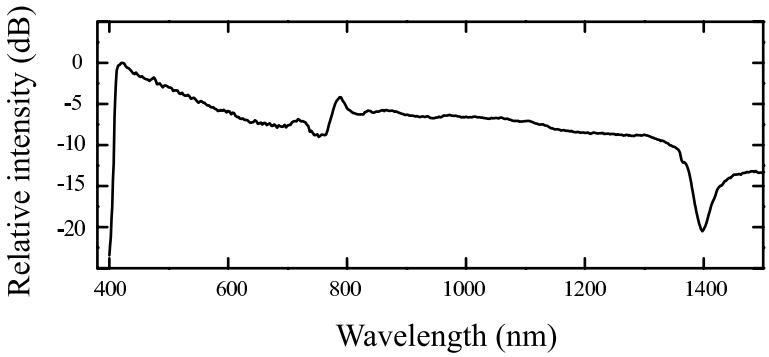

Figure 5.10: Measured spectrum of a supercontinuum produced in a microstructured optical fiber with structure parameters of $\Lambda = 1.47$ μm and $d/\Lambda = 0.74$. The zero dispersion wavelength of the fiber is at $\lambda_{ZDW} \approx 750$ nm. The pump laser has a wavelength of $\lambda_p = 780$ nm, a pulse length of $\Delta t = 6$ ns, and a peak power of $P_{peak} = 2$ kW. The fiber length is 20 m [IV].

5.4 Nondegenerate four-wave mixing

Four-wave mixing is called nondegenerate when the frequencies of the pump waves are not equal. In such a process two pump photons (ω_1 and ω_2) are annihilated and a signal (ω_s) and an idler photon (ω_i) are created. The conservation equations for the energy and the momentum are now

$$\omega_1 + \omega_2 = \omega_s + \omega_i \,, \tag{5.9}$$

and

$$\beta_1 + \beta_2 = \beta_s + \beta_i \,. \tag{5.10}$$

The principle and schematic spectrum of nondegenerate four-wave mixing are shown in Fig. 5.11. Similarly to degenerate four-wave mixing, the signal and idler frequencies are shifted equally in frequency from the pump waves. We can again develop the propagation constants $\beta_{s,i}$ into Taylor series. Equation (5.10) becomes

$$(\pm\beta_1^{(1)} \mp \beta_2^{(1)})\Omega + \frac{1}{2}(\beta_1^{(2)} + \beta_2^{(2)})\Omega^2 + \cdots = 0 \,, \tag{5.11}$$

where we have marked

$$\beta_m^{(n)} = \left.\frac{d^n\beta}{d\omega^n}\right|_{\omega=\omega_m} \,. \tag{5.12}$$

The upper signs in Eq. (5.11) apply when $\omega_i < \omega_2 < \omega_1 < \omega_s$, and the lower signs when $\omega_2 < \omega_i < \omega_s < \omega_1$. The leading term is now the difference of the first derivatives of

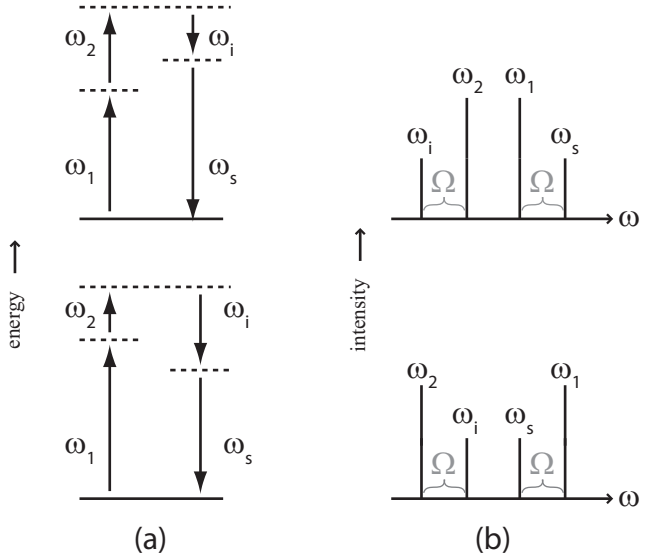

Figure 5.11: Principle (a) and schematic frequency spectrum of (b) nondegenerate four-wave mixing process for two cases $\omega_i < \omega_2 < \omega_1 < \omega_s$ (upper) and $\omega_2 < \omega_i < \omega_s < \omega_1$ (lower).

the propagation constants, evaluated at the pump wavelengths. These are the group delays, and a necessary condition for achieving phase-matching of nondegenerate four-wave mixing is thus a similar group delay at both pump wavelengths. This condition is equivalent to having the pump wavelengths spaced symmetrically around the zero-dispersion wavelength, one propagating in the normal dispersion and the other in the anomalous dispersion region. It is also the same condition as for cascaded cross-phase modulation, implying that nondegenerate four-wave mixing is observable with similar experimental conditions. Indeed, nondegenerate four-wave mixing was occasionally observed along with the cascaded XPM in [V], which led to [III].

The novelty in [III] is the demonstration of phase-matched nondegenerate four-wave mixing over a frequency bandwidth of more than one octave. The earlier publications on the topic work within a few nanometers in the normal dispersion region or within a few tens of nanometers centered at the zero-dispersion wavelength of the fiber [104, 105]. The increase in the bandwidth was made possible by the use of the pulsed high-peak power pump source, which allows for a short fiber length to be used, minimizing the dephasing

effect of the dispersion variation along the fiber length [106]. However, the longitudinal dispersion variation still remains as a limiting factor for the conversion efficiency [107], explaining why the conversion efficiency is reduced when the frequency separation of the signal and the idler waves is increased in [III].

Calculating the phase-matching diagram for the nondegenerate four-wave mixing is challenging because the signal and idler wavelengths are extremely sensitive to changes in the pump wavelengths. Shifting the pump wavelength by mere $\Delta\lambda = 1.2$ nm resulted in a more than $\Delta\lambda_s = 10$ nm change in the signal wavelength in [III]. The situation is equivalent to the case of pumping degenerate four-wave mixing slightly in the region of normal dispersion where the slope of the phase-matching curve is very steep (see Fig. 5.8). Due to this real physical sensitivity, the solution of the phase-matching equation (5.10) is highly sensitive to errors in the calculated propagation constant $\beta(\omega)$. The input data from which $\beta(\omega)$ is deduced are the pitch Λ and the hole size d of the fiber. Their values are determined from SEM micrographs of the fiber structure and thus prone to measurement errors. In addition, the real fiber structure is never perfectly periodic, as it is assumed in the calculation. The calculated phase-matching curves for nondegenerate FWM are thus good for qualitative analysis, but at best they give broad bands in which the signal and the idler wavelengths are likely to fit. The high sensitivity of the signal and idler wavelengths to the pump wavelengths can potentially be made use of in fiber optical parametric oscillators, so that tuning the pump by a couple of nanometers would scan the signal by tens of nanometers [106].

Nondegenerate four-wave mixing makes use of two pump waves, so that a similar two-dimensional phase-matching diagram as for degenerate four-wave mixing in Fig. (5.8) can not be plotted. However, this thesis considers miniature passively Q-switched lasers that can be easily frequency-doubled to put out two pump wavelengths that are separated by one octave, i.e., $\omega_1 = 2\omega_2$. In this special case a 2D phase-matching diagram can be plotted. Figure 5.12 shows such a diagram for a fiber with a pitch of $\Lambda = 1.35$ μm and a relative hole size of $d/\Lambda = 0.74$. The information is the same as in Fig. 2 of [III], but it is presented here in a more familiar way. As a comparison, the measured nondegenerate four-wave mixing spectrum of the fiber with a dual-wavelength pumping at $\lambda_1 = 532$ nm and $\lambda_2 = 1064$ nm is shown in Fig. 5.13. The two do not quite match quantitatively due to the aforementioned reasons, but they are in a qualitative agreement.

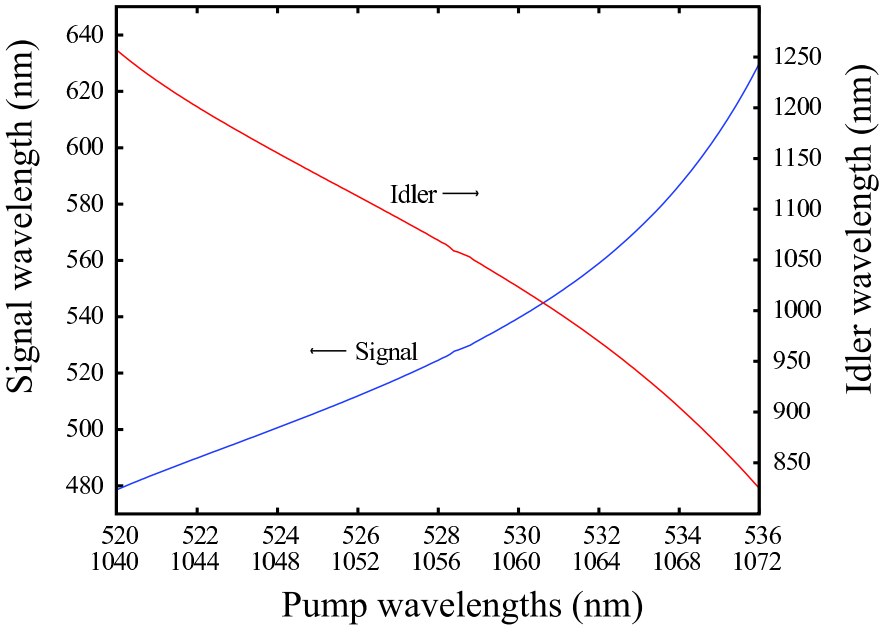

Figure 5.12: Calculated phase-matching diagram of nondegenerate four-wave mixing for a fiber with a pitch of $\Lambda = 1.35$ μm and a relative hole size of $d/\Lambda = 0.74$. The pump wavelengths are separated by one octave.

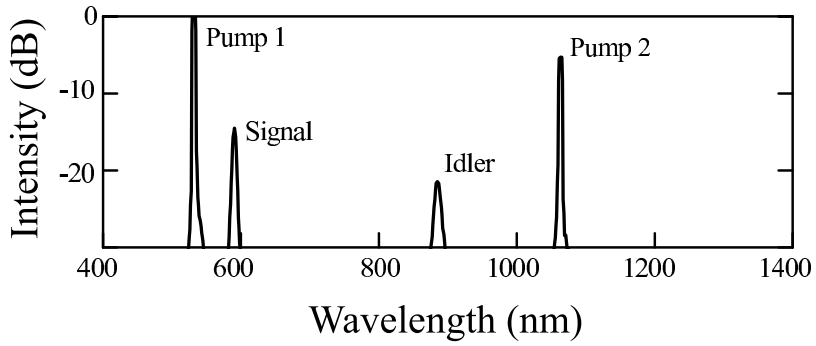

Figure 5.13: Measured nondegenerate four-wave mixing spectrum for a fiber with a pitch of $\Lambda = 1.35$ μm and a relative hole size of $d/\Lambda = 0.74$. The pump wavelengths are $\lambda_1 = 532$ nm and $\lambda_2 = 1064$ nm [III].

6 Summary and future outlook

The objective of this thesis has been to improve understanding of the operation of miniature passively Q-switched lasers and develop nonlinear fiber optical methods for converting the lasers' output spectra to new wavelengths. Both experimental and theoretical research has been carried into the lasers, and novel methods for nonlinear frequency conversion of nanosecond optical pulses in microstructured optical fibers have been demonstrated.

The normalized geometric rate-equation model of passively Q-switched lasers is extended in [I] to take into account the atomic response of the gain medium. The approach obviates the use of a constant inversion reduction factor, and allows the model to be applied to miniature lasers in which the cavity decay time and the thermalization time of the laser multiplets are at close to equal. The cavity mode and pump profiles are explicitly included in the model. The normalized pulse length of a passively Q-switched laser is found to diverge quickly, if the bleaching of the saturable absorber is slow ($\alpha \lesssim 10$) and the normalized thermalization rate falls below the value of one.

The newly developed numerical model is exploited in demonstrating a miniature passively Q-switched laser that emits pulses of yellow light [II]. The laser makes use of a standard 3 W laser diode as a pump source, and through frequency-doubling of the 1123 nm fundamental laser wavelength puts out pulses of 561 nm light with a peak power of 1 kW and a pulse length of 4 ns.

Numerical models of passively Q-switched lasers are still in a development process, as more complex approaches become feasible due to the constantly increasing computing power. The fundamental constrains of any numerical model however remain. Future modeling efforts would certainly benefit from more accurate data on the laser material parameters. The thermalization and relaxation time constants of most laser crystals are still unknown and await characterization in a systematic way. In addition, a large comparative study of the various models and their properties would help in choosing the best model for any specific task.

The lasers demonstrated in this thesis are quite small with their cavity lengths and crystal diameters being measured in some millimeters. However, there are many possibilities for making them even tinier. The longitudinal dimension can be reduced considerably by choosing a laser crystal with very high pump absorption and gain coefficients, such

as Nd:YVO_4, and using a semicondunductor based saturable absorber mirror (SESAM) instead of a bulk Q-switch crystal [108]. A shorter laser cavity produces also shorter pulses, which allows a higher repetition rate to be obtained with the given pump power. The disadvantage of a very short laser cavity is the equivalently small mode area, which prevents from producing large energy pulses. This can however be compensated with external optical amplification. It is likely that future miniature passively Q-switched laser sources are designed for some pulse length and repetition rate, and an external amplifier is used for growing the pulse energy. This kind of a laser source is more modular and allows for larger design freedom. The lateral dimensions of miniature lasers offer room for novel mechanical design solutions. The cavity mode is approximately a tenth of a millimeter wide, and if the transverse dimensions of the laser components could be reduced accordingly, the heat load of the laser crystal would be more easily dissipated and very low volume crystals could be used.

The second part of the thesis deals with nonlinear optical frequency conversion of nanosecond laser pulses in microstructured optical fiber. In publication [III], it is shown that nondegenerate four-wave mixing can be phase-matched over a frequency range of more than one octave in a small-core MOF, when nanosecond pump pulses are used. The output of a simple dual-wavelength source, a frequency-doubled and passively Q-switched Nd^{3+}:YAG laser, is converted into narrowband visible light the wavelength of which can be adjusted from blue to red by varying the structure of the fiber. In publication [IV], a low-cost device for producing visible supercontinuum light is demonstrated. A highly nonlinear microstructured optical fiber is pumped using a miniature gain-switched Ti:Sapphire laser, creating a spectrum that extends from 420 nm to 1300 nm within an amplitude variation of 8 dB. In publication [V], the process of cascaded cross-phase modulation is examined both experimentally and numerically. Cascaded XPM allows for generation of a smooth continuum of visible light, when visible and infrared pulses of light are co-propagated in a MOF at equal group velocities. A simple passively Q-switched and frequency-doubled Nd^{3+}:YAG laser works again as the pump source. The extent of the spectral broadening is found to be limited by the group delay profile of the fiber, which can be modified by changing the geometry of the fiber cladding.

The demonstrated sources emit light at visible and near-infrared wavelengths, but spectroscopic applications in ultraviolet and mid-infrared wavelengths could also make use of a high-brightness source of spatially coherent broadband light. On the blue side, the cut-off wavelength of cascaded cross-phase modulation could probably be extended down to

350 nm by further tailoring of the dispersion curve of the fiber. The possibility to change the geometry and hence the dispersion properties of microstructured optical fiber gives a large design freedom, which is largely unexploited at the present day. In this work fibers with only hexagonal cladding geometry are used, while far more complex alternatives have already been proposed [109]. However, extending the cascased XPM process to deeper UV wavelengths is hindered by the increasing material dispersion in UV that forbids the required group-velocity matching. Thus, at short UV wavelengths the spectral broadening of a nanosecond laser pulse can only rely on stimulated Raman scattering. Higher harmonics of infrared laser wavelenghths offer a large set of possible pump wavelengths down to 200 nm [56]. The challenges lie in producing a beam that is of sufficient quality for coupling into the fiber, and in the radiation damage of the fiber material. Silica glass is prone to solarization at wavelengths shorter than 340 nm (low-OH) and 270 nm (high-OH), which results in greatly increased loss and reduces the effective propagation length [91, 92]. Preferably, an alternative to silica glass should be found for ultraviolet wavelengths.

On the red-side, the extent of the spectral broadening in a fiber is limited by the multiphonon absorption edge of glass. In silica glass this boundary is found at close to 3 μm in wavelength, while number of glasses have a longer absorption edge, such as bismuth glass at 3.5 μm, fluoride glass at 4.5 μm, and chalcogenide glass at 7 μm [89,90]. Fluoride glass fiber has already been applied to broadband light generation with a cut-off wavelength at 4.5 μm [110]. The non-silica glasses feature also high nonlinearities which allows for shorter fiber lengths to be used in nonlinear applications [111]. The mid-infrared transparent nonsilica glasses are however “soft”. They melt at considerably lower temperatures than silica, and their damage threshold is lower. This can pose a problem for the use of passively Q-switched lasers as pump sources due to their relatively high pulse energies. Lower energies could be achieved by using semiconductor based saturable absorber mirrors, as discussed earlier. The SESAMs take close to no length in the laser cavity, which results in pulses that are both shorter and have lower energy, while the peak power is still high [108].

References

[1] J. J. Zayhowski and C. Dill III, "Diode-pumped passively Q-switched picosecond microchip lasers," Opt. Lett. **19**, 1427–1429 (1994).

[2] J. J. Zayhowski, "Passively Q-switched Nd:YAG microchip lasers and applications," J. of All. and Compounds **303–304**, 393–400 (2000).

[3] W. B. Lee, J. Y. Wu, Y. I. Lee, and J. Sneddon, "Recent applications of laser-induced breakdown spectrometry: A review of material approaches," Appl. Spect. Rev. **39**, 27–29 (2004).

[4] J. J. Zayhowski, "Miniature eye-safe laser system for high-resolution three-dimensional lidar," Appl. Opt. **48**, 5951–5956 (2007).

[5] L. J. Radziemsk, "From LASER to LIBS, the path of technology development," Spectrochim. Acta B **57**, 1109–1113 (2002).

[6] D. Y. Tang, S. P. Ng, L. J. Qin, and X. L. Meng, "Deterministic chaos in a diode-pumped Nd:YAG laser passively Q-switched by a Cr^{4+}:YAG crystal," Opt. Lett. **28**, 325–328 (2003).

[7] J. J. Degnan, D. B. Carry, and R. B. Kay, "Effects of thermalization on Q-switched laser properties," IEEE J. Quantum Electron. **34**, 887–899 (1998).

[8] L. V. Tarasov, *Laser Physics* (MIR, Moscow, 1983), 1st ed.

[9] J. A. F. Jr., "Ultrashort-pulse generation by Q-switched lasers," Phys. Rev. B **1**, 84–100 (1970).

[10] W. Koechner, *Solid-State Laser Engineering* (Springer-Verlag, Berlin, 1999), 5th ed.

[11] R. W. Boyd, *Nonlinear Optics* (Academic 'Press, New York, 2003), 2nd ed.

[12] J. K. Ranka, R. S. Windeler, and A. J. Stentz, "Visible continuum generation in air-silica microstructure optical fibers with anomalous dispersion at 800 nm," Opt. Lett. **25**, 25–27 (2000).

[13] W. Wadsworth, A. Ortigosa-Blanch, J. Knight, T. Birks, T. Man, and P. Russell, "Supercontinuum generation in photonic crystal fibers and optical fiber tapers: a novel light source," Journal of the Optical Society of America B **19**, 2148–2155 (2002).

[14] J. M. Dudley, G. Genty, and S. Coen, "Supercontinuum generation in photonics crystal fiber," Rev. M. Phys. **78**, 1135–1184 (2006).

[15] P. Kelkar, F. Coppinger, A. Bhushan, and B. Jalali, "Time-domain optical sensing," Electronics Letters **35**, 1661–1662 (1999).

[16] C. F. Kaminski, R. S. Watt, A. D. Elder, J. H. Frank, and J. Hult, "Supercontinuum radiation for applications in chemical sensing," Appl. Phys. B **92**, 367–378 (2008).

[17] K. Lindfors, T. Kalkbrenner, P. Stoller, and V. Sandoghdar, "Detection and spectroscopy of gold nanoparticles using supercontinuum white light confocal microscopy," Phys. Rev. Lett. **93**, 037401 (2004).

[18] T. Ritari, G. Genty, and H. Ludvigsen, "Supercontinuum and gas cell in a single microstructured fiber," Optics Letters **30**, 3380–3382 (2005).

[19] G. R. Hadley, A. Owyoung, P. Esherik, and J. P. Hohimer, "Numerical simulation and experimental studies of longitudinally excited miniature solid-state lasers," Appl. Opt. **27**, 819–827 (1988).

[20] J. G. Endriz, M. Vakili, G. S. Browder, M. DeVito, J. M. Haden, G. L. Harnagel, W. E. Plano, M. Sakamoto, D. F. Welch, and S. Willing, "High power diode laser arrays," IEEE J. Quantum Electron. **28**, 952–965 (1992).

[21] W. G. Wagner and B. A. Lengyel, "Evolution of the giant pulse in a laser," J. Appl. Phys. **34**, 2040–2046 (1963).

[22] S. Singh, R. G. Smith, and L. G. V. Uitert, "Stimulated-emission cross section and fluorescent quantum efficiency of Nd^{3+} in yttrium aluminum garnet at room temperature," Phys. Rev. B **10**, 2566–2572 (1974).

[23] J. Morikawa, T.Hashimoto, T. Ogawa, S. Wada, and M. Higuchi, "Thermal conductivity/diffusivity of Nd^{3+} doped $GdVO_4$, YVO_4, $LuVO_4$ and $Y_3Al_5O_{12}$

measured by temperature wave method," in "Conference on Lasers and Electro-Optics," (OSA, 2007).

[24] J.-Y. Ko, C.-C. Lin, K. Otsuka, Y. Miyasaka, K. Kamikariya, K. Nemoto, M.-C. Ho, and I.-M. Jiang, "Experimental observations of dual-polarization oscillations in laser-diode-pumped wide-aperture thin-slice Nd:$GdVO_4$ lasers," Opt. Expr. **15**, 945–954 (2007).

[25] J. Liu, J. Yang, and J. He, "Diode-pumped passively Q-switched c-cut Nd:$GdVO_4$ laser," Opt. Comm. **219**, 317–321 (2003).

[26] T. Jensen, V. G. Ostroumov, J.-P. Meyn, G. Huber, A. I. Zagumennyi, and I. A. Shcherbakov, "Spectroscopic characterization and laser performance of diode-laser-pumped Nd:$GdVO_4$," Appl. Phys. B **58**, 373–379 (1994).

[27] Y. Sato and T. Taira, "Thermo-optical and mechamical parameters of Nd:$GdVO_4$ and Nd:YVO_4," in "Conference on Lasers and Electro-Optics," (2007).

[28] O. Svelto, *Principles of Lasers* (Plenum Press, New York, 1998), 4th ed.

[29] P. F. Moulton, "Spectroscopic and laser characteristics of Ti:Al_2O_3," J. Opt. Soc. Am. B **3**, 125–133 (1986).

[30] T. H. Maiman, "Stimulated optical radiation in Ruby," Nature **187**, 493–494 (1960).

[31] P. Lacovara, H. K. Choi, C. A. Wang, R. L. Aggarwal, and T. Y. Fan, "Room-temperature diode-pumped Yb:YAG laser," Opt. Lett. **16**, 1089–1091 (1991).

[32] J. E. Geusic, H. M. Marcos, and L. G. V. Uitert, "Laser oscillations in Nd-doped yttrium aluminum, yttrium gallium and gadolinium garnets," Appl. Phys. Lett. **4**, 182–184 (1964).

[33] E. V. Zharikov, V. I. Zhekov, L. A. Kulevskii, T. M. Murina, V. V. Osiko, A. M. Prokhorov, A. D. Savel'ev, V. V. Smirnov, B. P. Starikov, and M. I. Timoshechkin, "Stimulated emission from Er^{3+} ions in yttrium aluminum garnet crystals at $\lambda = 2.94$ μm," Sov. J. Quantum Electron. **4**, 1039–1040 (1975).

[34] B. Aull and H. Jenssen, "Vibronic interactions in Nd:YAG resulting in nonreciprocity of absorption and stimulated emission cross sections," IEEE J. Quantum Electron. **18**, 925–930 (1982).

[35] S. V. Voitikov, A. A. Demidovich, L. E. Batay, A. N. Kuzmin, and M. B. Danailov, "Sub-nanosecond pulse dynamics of Nd:LSB microchip laser passively Q-switched by Cr:YAG saturable absorber," Opt. Comm. **251**, 154–164 (2005).

[36] H. E. Türeki, L. Ge, S. Rotter, and A. D. Stone, "Strong interactions in multimode random lasers," Science **320**, 643–646 (2008).

[37] K. Kubodera, K. Otsuka, and S. Miyazawa, "Stable $LiNdP_4O_{12}$ miniature laser," Appl. Opt. **18**, 884–490 (1979).

[38] M. A. Larotonda, A. M. Yacomotti, and O. E. Martínez, "Antiphase Q-switch dynamics in a multimode solid-state laser with saturable absorber," Opt. Comm. **169**, 149–158 (1999).

[39] J. Dong and K. Ueda, "Longitudinal-mode competition induced instabilities of Cr^{4+},Nd^{3+}:$Y_3Al_5O_{12}$ self-Q-switched two-mode laser," Appl. Phys. Lett. **87**, 151102 (2005).

[40] X. Zhang, S. Zhao, Q. Wang, B. Ozygus, and H. Weber, "Modeling of passively Q-switched lasers," J. Opt. Soc. Am. B **17**, 1166–1175 (2000).

[41] B. E. A. Saleh and M. C. Teich, *Fundamental of Photonics* (Wiley, 2007), 2nd ed.

[42] B. Boulanger, M. M. Fejer, R. Blachman, and P. F. Bordui, "Study of $KTiOPO_4$ gray-tracking at 1064, 532, and 355 nm," Appl. Phys. Lett. **65**, 2401 (1994).

[43] B. Boulanger, I. Rousseau, J. P. Feve, M. Maglione, B. Menaert, and G. Marnier, "Optical studies of laser-induced gray-tracking in KTP," IEEE J. Quantum Electron. **35**, 281–286 (1999).

[44] I. Y. Milev, S. S. Dimov, D. V. Terziev, J. I. Iordanova, L. B. Todorova, and A. B. Gelkova, "Laser-induced damage threshold measurements of optical dielectric coatings at $\lambda = 1.06$ μm," J. Appl. Phys. **70**, 4057–4059 (1991).

[45] W. H. Lowdermilk and D. Mila, "Laser-induced surface and coating damage," IEEE J. Quantum Electron. **17**, 1888–1903 (1981).

[46] A. A.Kaminskii and H. F. Ivey, *Laser Crystals: Their Physics and Properties* (Springer-Verlag, 1981).

[47] B. L. Volodin, S. V. Dolgy, E. D. Melnik, E. Downs, J. Shaw, and V. S. Ban, "Wavelength stabilization and spectrum narrowing of high-power multimode laser diodes and arrays by used of volume Bragg gratings," Opt. Lett. **29**, 1891–1893 (2004).

[48] Y. Shimony, Z. Burshtein, and Y. Kalinsky, "Cr^{4+}:YAG as passive Q-switch and brewster plate in a pulsed Nd:YAG laser," IEEE J. Quantum Electron. **31**, 1738–1741 (1995).

[49] A. Agnesi, S. Morello, C. Piccinno, G. Reali, and G. Sun, "Diode-pumped Neodymium lasers repetitively Q-switched by Cr^{4+}:YAG solid-state saturable absorbers," IEEE J. Sel. Top. Quantum Electron. **3**, 45–52 (1997).

[50] Z. Burshtein, P. Blau, Y. Kalinsky, Y. Shimony, and M. R. Kokta, "Excited-state absorption studies of Cr^{4+} ions in several garnet host crystals," IEEE J. Quantum Electron. **34**, 292–299 (1998).

[51] B. Henderson, H. G. Gallagher, T. P. J. Han, and M. A. Scott, "Optical spectroscopy and optimal crystal growth of some Cr^{4+}-doped garnets," J. Phys.: Condens. Matter **12**, 1927–1938 (2000).

[52] H. Ridderbusch and T. Graaf, "Saturation on 1047- and 1064-nm absorption in Cr^{4+}:YAG crystals," IEEE J. Quantum Electron. **43**, 168–173 (2007).

[53] A. Sennaroglu, U. Demirbas, S. Ozharar, and F. Yaman, "Accurate determination saturation parameters for Cr^{4+} -doped solid-state saturable absorbers," J. Opt. Soc. Am. B **23**, 241–249 (2006).

[54] J. J. Zayhowski, S. C. Buchter, and A. L. Wilson, "Miniature gain-switched lasers," OSA Trends in Optics and Photonics **50**, 462–469 (2001).

[55] G. D. Boyd and D. A. Kleinman, "Parametric interaction of focused Gaussian beams," J. Appl. Phys. **39**, 3597–3639 (1968).

[56] J. J. Zayhowski, "Ultraviolet generation with passively Q-switched microchip lasers," Opt. Lett. **21**, 588–590 (1996).

[57] A. Agnesi, S. D. Acqua, E. Piccinini, G. Reali, and G. Piccinno, "Efficient wavelength conversion with high-power passively-switched diode-pumped Neodymium lasers," IEEE J. Quantum Electron. **34** (1998).

[58] V. Pasiskevicius, S. Wang, J. A. Tellefsen, F. Laurell, and H. Karlsson, "Efficient Nd:YAG laser frequency doubling with periodically poled KTP," Appl. Opt. **37**, 7116–7119 (1998).

[59] F. Laurell, "Periodically poled materials for miniature light sources," Opt. Mat. **11**, 235–244 (1999).

[60] AS Photonics, *SNLO computer program and the references within: www.as-photonics.com*.

[61] K. Kato, "Second-harmonic and sum-frequency generation in $KTiOAsO_4$," IEEE J. Quantum Electron. **30**, 881–883 (1994).

[62] J. J. Degnan, "Optimization of passively Q-switched lasers," IEEE J. Quantum Electron. **31**, 1890–1901 (1995).

[63] G. Xiao and M. Bass, "A generalized model for passively Q-switched lasers including excited state absorption in the saturable absorber," IEEE J. Quantum Electron. **33**, 41–44 (1997).

[64] S. T. Li, X. Y. Zhang, Q. P. Wang, P. Li, J. Chang, X. L. Zhang, and Z. H. Cong, "Modeling of Q-switched lasers with top-hat pump beam distribution," Appl. Phys. B **88**, 221–226 (2007).

[65] S. R. Chinn and V. King, "Subnanosecond (Er,Yb) glass Q-switched microlasers: 3-D transient modeling and experiments," IEEE J. Quantum Electron. **42**, 1128–1136 (2006).

[66] G. L. McAllister, M. M. Mann, and L. G. DeShazer, "Transverse-mode distortions in giant-pulse laser oscillators," IEEE J. Quantum Electron. **1**, 44–48 (1970).

[67] W. W. Rigrod, "Saturation effects in high gain lasers," J. Appl. Phys. **36**, 2487–2490 (1965).

[68] A. A. Grütter and H. Weber, "Pulse shaping effects in Q-switched laser oscillators," Opt. Quantum Electron. **3**, 13–18 (1971).

[69] D. H. Stone, "Effects of axial nonuniformity in modeling Q-switched lasers," IEEE J. Quantum Electron. **28**, 1970–1973 (1992).

[70] C. D. Nabors, “Q-switched operation of quasi-three-level lasers,” IEEE J. Quantum Electron. **30**, 2896–2901 (1994).

[71] J. Swiderski, A. Zajac, P. Konieczny, and M. Skorczakowski, “Numerical model of a Q-switched double-clad fiber laser,” Opt. Expr. **12**, 3554–3559 (2004).

[72] I. Laukaitytė and R. Čiegis, “Finite-difference scheme for one problem in nonlinear optics,” Math. Mod. and Anal. **13**, 211–222 (2008).

[73] J. J. Degnan, “Theory of the optimally coupled Q-switched laser,” IEEE J. Quantum Electron. **25**, 214–220 (1989).

[74] D. Li, S. Zhao, G. Li, and K. Yang, “Optimization of peak power of passively Q-switched lasers by taking into account intracavity laser spatial distribution,” Opt. & Las. Tech. **39**, 13–20 (2007).

[75] L. R. de and B. Westergren, *Mathematic Handbook for Science and Engineering* (Studentlitteratur, Lund, 2001), 1st ed.

[76] J. J. Degnan and J. J. Zayhowski, “SLR2000 Microlaser performance: Theory vs Experiment,” Proc. of 11th International Workshop on Laser Ranging, pp. 453–468 (1998).

[77] A. E. Siegman, *Lasers* (University Science Books, Mill Valley, 1986), 1st ed.

[78] G. L. McAllister and M. M. Mann and L. G. DeShazer, “Transverse-mode distortions in giant-pulse laser oscillators,” IEEE J. Quantum Electron. **1**, 44–48 (1969).

[79] J. Dong, A. Shirakawa, and K. Ueda, “Switchable pulses generation in passively Q-switched multi longitudinal-mode microchip laser,” Las. Phys. Lett. **4**, 109–116 (2007).

[80] J. C. Knight, T. A. Birks, P. S. J. Russell, and D. M. Atkin, “All-silica single-mode optical fiber with photonic crystal cladding,” Opt. Lett. **21**, 1547–1549 (1996).

[81] P. Russell, “Photonic crystal fibers,” Science **299**, 358–362 (2003).

[82] G. P. Agrawal, *Nonlinear Fiber Optics* (Academic Press, San Diego, 1995), 2nd ed.

[83] F. Zolla, G. Renversez, A. Nicolet, S. G. B. Kuhlmey, and D. Felbackq, *Foundations of Photonic Crystal Fibers* (Imperial College Press, London, 2005), 1st ed.

[84] J. C. Knight, J. Arriaga, T. A. Birks, A. Ortigosa-Blanch, W. J. Wadsworth, and P. S. J. Russell, "Anomalous dispersion in photonic crystal fiber," Photon. Technol. Lett. **12**, 807–809 (2000).

[85] Univ. of Sydney, *CUDOS MOF software package: www.physics.usyd.edu.au/cudos/mofsoftware/*.

[86] K. L. Reichenbach and C. Xu, "The effects of randomly occurring nonuniformities on propagation in photonic crystal fibers," Opt. Expr. **13**, 2799–2807 (2005).

[87] T. P. White, B. T. Kuhlmey, R. C. McPhedran, D. Maystre, G. Renversez, C. M. de Sterke, and L. C. Botten, "Multipole method for microstructured optical fibers. I: Formulation," J. Opt. Soc. Am. B **19**, 2322–2330 (2002).

[88] B. T. Kuhlmey, T. P. White, G. Renversez, D. Maystre, L. C. Botten, C. M. de Sterke, and R. C. McPhedran, "Multipole method for microstructured optical fibers. II: Implementation and results," J. Opt. Soc. Am. B **19**, 2331–2340 (2002).

[89] T. M. Monro and H. Ebendorff-Heidepriem, "Progress in microstructured optical fibers," Ann. Rev. Mat. Research **36**, 467–495 (2006).

[90] J. H. V. Price, T. M. Monro, H. Ebendorff-Heidepriem, F. Poletti, P. Horak, V. Finazzi, J. Y. Y. Leong, P. Petropoulos, J. C. Flanagan, G. Brambilla, X. Feng, and D. J. Richardson, "Mid-IR supercontinuum generation from nonsilica microstructured optical fibers," IEEE J. Quantum Electron. **13**, 738–759 (2007).

[91] P. Karlitschek, G. Hillrichs, and K.-F. Klein, "Influence of hydrogen on the colour center formation in optical fibers induced by pulsed UV-laser radiation. Part 1: all silica fibers with high-OH undoped core," Opt. Comm. **155**, 376–385 (1998).

[92] P. Karlitschek, G. Hillrichs, and K.-F. Klein, "Influence of hydrogen on the colour center formation in optical fibers induced by pulsed UV-laser radiation. Part 2: all silica fibers with low-OH undoped core," Opt. Comm. **155**, 386–397 (1998).

[93] K. Kurokawa, K. Tajima, K. Tsujikawa, and K. Nakajima, "Reducing the losses in photonic crystal fibers," Proc. of ECOC **2**, 279–282 (2005).

[94] P. J. Roberts, F. Couny, H. Sabert, B. J. Mangan, T. A. Birks, J. C. Knight, and P. S. J. Russell, "Loss in solid-core photonic crystal fibers due to interface roughness scattering," Opt. Expr. **13**, 7779–7793 (2005).

[95] U. Keller, "Recent developments in compact ultrafast lasers," Nature **424**, 831–838 (2003).

[96] C. Chedot, C. Lecaplain, S. Idlahcen, G. Martel, and A. Hideur, "Mode-locked ytterbium-doped fiber lasers: New perspectives context sensitive links," Fiber Integ. Opt. **27**, 341–354 (2008).

[97] S. Buchter, M. Kaivola, H. Ludvigsen, and K. P. Hansen, "Miniature supercontinuum laser sources," CLEO Tech. Digest, p. CTuP58 (2004).

[98] N. R. Newbury, "Pump-wavelength dependence of Raman gain in single-mode optical fibers," J. Lightwave Technol. **21**, 3364–3373 (2003).

[99] J. P. Gordon, "Theory of the soliton self-frequency shift," Opt. Lett. **11**, 662–664 (1986).

[100] G. Genty, M. Lehtonen, and H. Ludvigsen, "Route to broadband blue-light generation in microstructured fibers," Opt. Lett. **30**, 756–758 (2005).

[101] T. Schreiber, T. V. Andersen, D. Schimpf, J. Limbert, and A. Tünnermann, "Supercontinuum generation by femto-second single and dual wavelength pumping in photonic crystal fibers with two zero dispersion wavelengths," Opt. Expr. **13**, 9556–9569 (2005).

[102] A. Y. H. Chen, G. K. L. Wong, S. G. Murdoch, R. Leonhardt, J. D. Harvey, J. C. Knight, W. J. Wadsworth, and P. S. J. Russell, "Widely tunable optical parameteric generation in a photonic crystal fiber," Opt. Lett. **30**, 762–764 (2005).

[103] W. J. W. andN. Joly, J. C. Knight, T. A. Birks, and P. S. J. Russell, "Supercontinuum and four-wave mixing with Q-switched pulses in endlessly single-mode photonic crystal fibres," Opt. Expr. **12**, 299–309 (2004).

[104] J. R. Thompson and R. Roy, “Nonlinear dynamics of multiple four-wave mixing processes in a single-mode fiber,” Phys. Rev. A **43**, 4987–4996 (1991).

[105] K. Inoue, “Tunable and selective wavelength conversion using fiber four-wave mixing with two pump lights,” Photon. Technol. Lett. **6**, 1451–1453 (2007).

[106] J. D. Harvey, S. G. Murdoch, S. Coen, R. Leonhardt, D. Mechin, and G. K. L. Wong, “Parametric processes in microstructured and highly nonlinear optical fibres,” Opt. Quantum Electron. **39**, 1103–1114 (2007).

[107] R. H. Stolen and J. E. Björkholm, “Parametric amplification and frequency conversion in optical fibers,” IEEE J. Quantum Electron. **18**, 1062–1072 (1982).

[108] G. J. Spühler, R. Paschotta, R. Fluck, B. Braun, M. Moser, G. Zhang, E. Gini, and U. Keller, “Experimentally confirmed design guidelines for passively Q-switched microchip lasers using semiconductor saturable absorbers,” J. Opt. Soc. Am. B **16**, 376–388 (1999).

[109] W. Q. Zhang, V. A. Shahraam, and T. M. Monro, “Optimizing the bandwidth and coherence of supercontinuum in soft glass microstructured fibers,” CLEO Tech. Digest, p. CMDD5 (2008).

[110] C. Xia, M. Kumar, O. P. Kulkarni, M. N. Islam, F. L. T. Jr., M. J. Freeman, M. Poulain, and G. Mazé, “Mid-infrared supercontinuum generation to 4.5 μm in ZBLAN fluoride fibers by nanosecond diode pumping,” Opt. Lett. **31**, 2553–2555 (2006).

[111] J. Y. Y. Leong, P. Petropoulos, J. H. V. Price, H. Ebendorff-Heidepriem, S. Asimakis, R. C. Moore, K. E. Frampton, V. Finazzi, X. Feng, T. M. Monro, and D. J. Richardson, “High-nonlinearity dispersion-shifted lead-silicate holey fibers for efficient 1-μm pumped supercontinuum generation,” J. Lightwave Technol. **24**, 183–190 (2006).

ISBN 978-951-22-9982-9
ISBN 978-951-22-9983-6 (PDF)
ISSN 1795-2239
ISSN 1795-4584 (PDF)